TEM investigation on Challapampa aquifer, Oruro Bolivia

Måns Larsson

Dissertations in Geology at Lund University,
Master's thesis, no 494
(45 hp/ECTS credits)

Department of Geology
Lund University
2016

LUNDS TEKNISKA HÖGSKOLA
Lunds universitet

Lund University
Faculty of Engineering, LTH
Departments of Earth and Water Engineering

This study has been carried out within the framework of the Minor Field Studies (MFS) Scholarship Programme, which is funded by the Swedish International Development Cooperation Agency, Sida.

The MFS Scholarship Programme offers Swedish university students an opportunity to carry out two months' field work in a developing country resulting in a graduation thesis work, a Master's dissertation or a similar in-depth study. These studies are primarily conducted within subject areas that are important from an international development perspective and in a country supported by Swedish international development assistance.

The main purpose of the MFS Programme is to enhance Swedish university students' knowledge and understanding of developing countries and their problems. An MFS should provide the student with initial experience of conditions in such a country. A further purpose is to widen the human resource base for recruitment into international co-operation. Further information can be reached at the following internet address: http://www.tg.lth.se/mfs

The responsibility for the accuracy of the information presented in this MFS report rests entirely with the authors and their supervisors.

Gerhard Barmen

Gerhard Barmen
Local MFS Programme Officer

Postadress Box 118, 221 00 Lund *Besöksadress* John Ericssons väg 1*Telefon dir* 046-222 9657, *växel* 046-222 00 00 *Telefax* 046-2229127
E-post Gerhard.Barmen@tg.lth.se

TEM investigation on Challapampa aquifer, Oruro Bolivia

Master's thesis

Måns Larsson

Department of Geology
Lund University
2016

Table of contents

Cover Picture: The WalkTEM instrument during one of the field days on the Bolivian altiplano. Photo Måns Larsson.

English abstract

MÅNS LARSSON

Larsson, m., 2016: TEM investigation on Challapampa aquifer, Oruro Bolivia. *Dissertations in Geology at Lund University*, No. 494, 44 pp. 45 hp (45 ECTS credits) .

Abstract:

In this study a TEM (transient electromagnetic) investigation where preformed on the Bolivian altiplano north of the city Oruro. There is a deficit of drinking water in Oruro and the aquifer Challapampa is their main source of water. With this investigation the objective was to map the bottom limitation of the Challapampa aquifer and, if possible, restraining structures within the aquifer, aquitards. The surrounding bedrock consists mainly of sandstones and shale's that has been penetrated by intrusions in several locations. Quaternary sediments on top of the bedrock hold most of the groundwater in the area. The general structures in the bedrock surrounding the Quaternary sediments are in a northwest to southeast direction and similar structures are expected to be found underneath the sediments.

The method used in this investigation was TEM, which uses transient electromagnetic (EM) waves to penetrate the ground. TEM is a geophysical technique that creates a magnetic field by passing an electrical current through an ungrounded cable. When the current is cut off, as quickly as possible, the magnetic field induces a current in its surrounding ground that results in a secondary magnetic field. The secondary magnetic field induces a current in the receiver antenna and electrical potentials are measured and registered in the instrument. The variation of the secondary magnetic field depends on the ground properties.

The TEM method is well suited for investigating groundwater properties in sand- and gravel-dominated deposits. A depth of investigation (DOI) to 850 m b.s. (meters below surface) was achieved in several points, which is over expectations. Two low resistivity valleys were found and interpreted as water saturated sedimentary valleys, where extend in a northwest to southeast direction over the studied area. The depth to the bedrock is interpreted to be around 75 m b.s., both in the western and eastern part of the area. The basal boundary for the interpreted sedimentary valleys crossing profile 3 (NorthH2, Fig. 24) is around 130 m b.s. for the eastern valley and 120 m b.s. for the western valley.

Keywords: Geophysics, Hydrogeology, Geology, Sedimentary, Survey

Supervisor(s): Per Möller, Torleif Dhalin

Subject: Geology, Geophysics

Måns Larsson, Department of Geology, Lund University, Sölvegatan 12, SE-223 62 Lund, Sweden. E-mail: mablarsson@gmail.com

Svensk abstract

MÅNS LARSSON

Larsson, M., 2016: TEM investigation on Challapampa aquifer, Oruro Bolivia. *Examensarbeten i geologi vid Lunds universitet*, Nr. 494, 44 sid. 45 hp.

Sammanfattning:

I denna studie utfördes en TEM (transient elektromagnetisk) undersökning på den Bolivianska altiplanon, norr om staden Oruro. I Oruro finns det ett underskott av dricksvatten och deras huvudsakliga vattenförsörjning kommer från aquiferen Challapampa. Målet med undersökningen var att kartlägga djup till bottnen på aqviferen, topografin av botten samt, om möjligt, akvitarder innom akviferen. De omkringliggande berget består av sandsten, skiffer och intrusioner. Ovanpå berget finns det Kvartära avlagringar som innehåller de största grundvattenreserverna. I det omkringliggande berget sträcker sig strukturer från nordväst till sydöst, och det är förväntat att strukturer med samma trend ska återfinnas på botten av akvifären, men även strukturer kopplade till de intrusioner som finns.

TEM metoden är en transient elektromagnetisk sonderings metod som använder elektromagnetiska vågor för att undersöka marken. Ett magnetisktfält skapas när elektrisitet leds genom en kabel på marken. När strömmen stängs av induceras en elektromotorisk kraft ner i marken som inducerar virvelströmmar i lager med avvikande elektrisk ledningsförmåga. Virvelströmmarna skapar i sin tur ett sekundärt magnetfält som inducerar ström i mottagarspolen. Det sekundära magnetfältet varierar med markens elektriska ledningsförmåga och innehåller på så sätt information om markens fysiska egenskaper.

TEM metoden var väl lämpad för att undersöka hydrogeologiska egenskaper i en sand- och grus-dominerad avlagring. Ett större undersökningsdjup än väntat uppnåddes på 850 m under markytan i flera mätpunkter. Två lågresistiva dalar, som sträcker sig i en nordväst till sydöstlig riktning, hittades. Dalarna är tolkade att innehålla vattenmättade sediment. Djupet till berggrund i undersökningsområdets, absolut västra samt östra delar, är tolkat att vara cirka 75 m under markytan, medans djupet till berg i de tolkade dalarna är ca 130 m under markytan i den östra dalen och 120 m under markytan i den västra dalen.

Nyckelord: Geofysik, Hydrogeologi, Geologi, Sedimentologi, Kartering,

Handledare: Per Möller, Torleif Dahlin

Ämnesinriktning: Geologi, Geofysik

Måns Larsson, Geologiska institutionen, Lunds Universitet, Sölvegatan 12, 223 62 Lund, Sverige. E-post: mablarsson@gmail.com

1 Introduction

This Master's thesis is written at the Geology department, Lund's university and in cooperation with LTH – Engineering Geology. The objective of this study was to map the bottom limitation of the Challapampa aquifer that is located adjacent to the city Oruro on the Bolivian altiplano. The aquifer is mainly situated in Quaternary sediments within an alluvial fan. The surrounding bedrock consist of shale's, sandstone and intrusive rock. It is expected to find bedrock as the bottom limitation of the aquifer and structures similar to those in the surrounding mountains. Most recharging to the aquifer consists of run off from surrounding mountainous terrain and is transported to the area via rivers. The method used for this survey is TEM, which is a transient electromagnetic method. This method is relatively new and has been used in Denmark to map groundwater resources. The method uses short pulses of current to create an electromotive force that propagate down in the subsurface inducing eddy current in layers with deviating resistivity and emitting secondary magnetic fields back to the receiver on the surface. The secondary magnetic field properties depend on the ground properties, and contain thereby information about the subsurface. Upsides with the TEM-method are; the deep depth of investigation (DOI), fast setup and measuring time, point based surveys giving the possibility for customized designer grids and sensitivity in detecting and mapping low resistivity formations.

The survey was carried out by me (Måns Larsson) and Etzar Gómez during an eight week long field campaign. During the campaign we lived in an apartment in Oruro and went to the field area by a natural gas powered taxi. To transport the equipment between the measuring points within the field area a bicycle cart was used. As help in the field, two students from Technical University of Oruro (UTO), Rafael Mendoza Huayhua and Jorge Larrea, was recruited, taught basic theory behind the method and setting up the instrument.

After the field campaign, in the post data gathering and evaluation process, the program ViewTEM was used to sort the data and make it ready for visualisation in Aarhus Workbench. In Workbench a series of horizontal maps and profiles where produced to visualise the results of the survey. These maps were used as base in the discussion to draw the conclusions of this report.

2 Study area

The study area is located 15 km northeast from Oruro city (Fig. 1) in Bolivia, South America. The area is bounded by latitudes 17°35'–18°00' S and longitudes 66°59'–67°12' W. The topography in the study area is flat, plateau-like, with an average elevation of 3 700 m a.s.l. The surrounding landscape is mountainous, with peaks reaching 4 700 m a.s.l. and characterized by a semiarid climate throughout the plateau and in the surrounding mountains. The vegetation is scarce or almost non-existent due to the semi-arid climate and the high elevation. The mean annual temperature is about 10°C and shows large differences between day and night. The rainfall is in the range of 300 to 500 mm/y, with a markedly wet summer from December to March, and dry winter from June to August. Quaternary sediments hold most groundwater in the area and are part of the Oruro-Caracollo hydrologic catchment, forming the Challapampa aquifer with an area of ca. 525 km^2.

3 Background

The Challapampa aquifer is located on the Bolivian altiplano adjacent to Oruro. The city Oruro is dependent on water supply from this aquifer and at the moment of writing the water supplied to the city is not enough to cover the needs of its inhabitants. Among the local farmers north of Oruro there is a high suspicion against both the water company and foreigners making investigations in the area. A fear of running

Fig. 1. Overview of the study area in Bolivia.

out of water and that outsiders will mark their land for commercial use are some of the reasons for this general attitude. This has somewhat limited our investigations in the area since we were not allowed to make coherent measurements as wished for. The eastern limitation of our investigation area (Fig. 2) is mountainous terrain and exposed bedrocks, which is not the target of the study.

The general groundwater flow is from north to south and the local recharge source except of rain is the Paria River. The investigated area is located in a desert with high salt content, both on the surfaces and within clay layers on greater depth. During the dry season the evaporation is very high and salt precipitation over ground surfaces is large (Fig. 3), especially in the eastern part of the investigated area, close to the natural hot springs (Fig. 2) which produce highly saline water (360 mS/m or 2.8 Ω m).

3.1 Bedrock geology

The San José mine is located directly west of Oruro in an elevated hill complex, called the Oruro massif. It is an old mine that have produced tin, silver and lead as the main metals during the last 400 years. The most common minerals in the intrusion are listed by Patureau (2007), and are silica (SiO_2), cassiterite

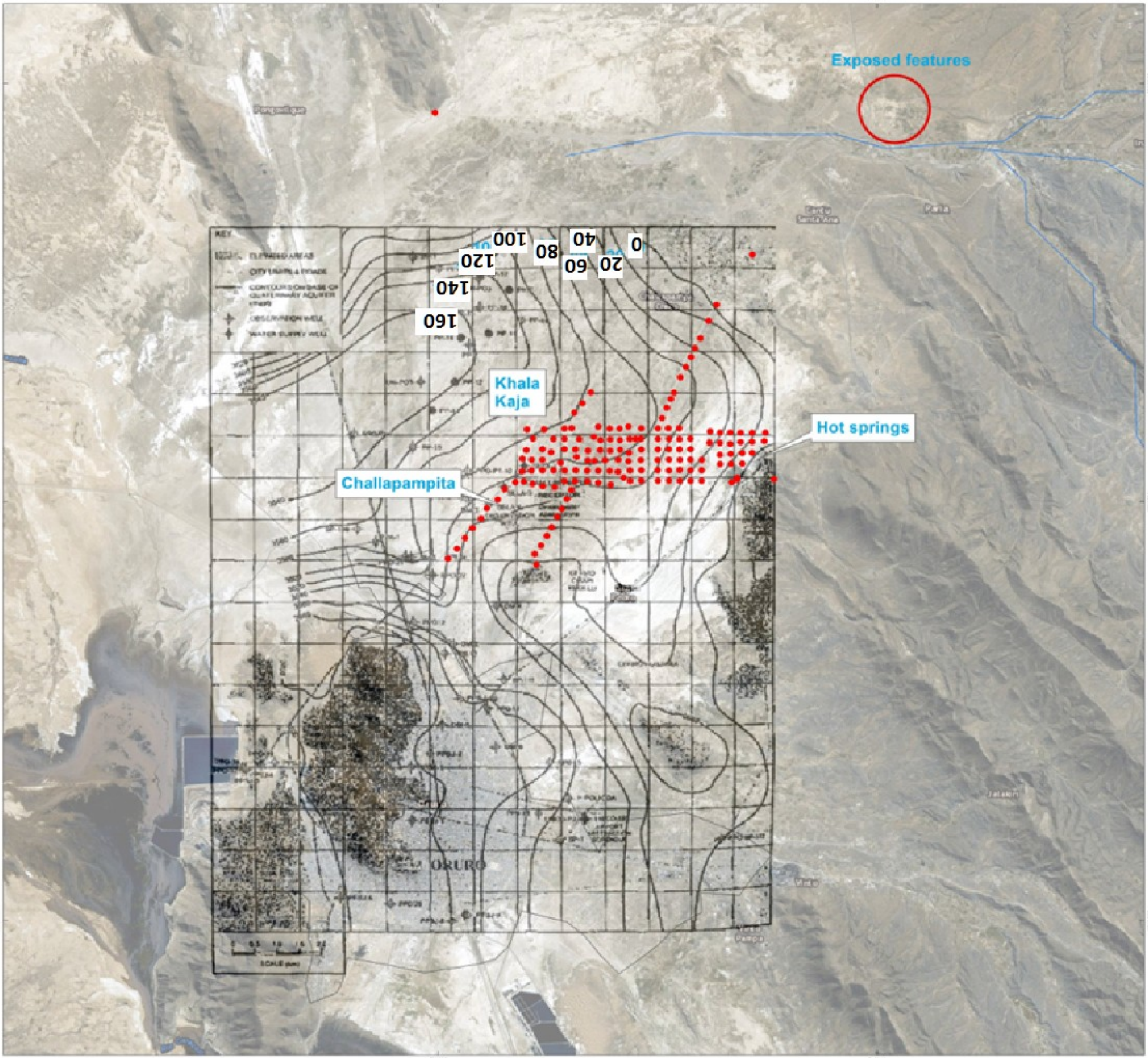

Fig. 2. This is a contour map put on top of the investigated area showing an interpretation of the top bedrock surface. Red dots are TEM measurements and black dots are previous geophysical investigations and boreholes. The PP_ boreholes are located within the Khala Kaja area and the Sela well field are located within Challapampita. The contours for the bedrock surface are based on information from Banks et al. (2002).

Fig. 3. Precipitated salt on top of the clayey sedimentary strata. Photo by Måns Larsson.

(SnO_2), pyrite (FeS_2), estannine (Cu_2FeSnS_4), tetrahedrite ($(Cu,Fe,Ag,Hg,Zn)_7(Sb,As)_2S_8$), andorite ($AgPbSb_3S_6$), zinkenite ($PbSb_2S_4$) and boulangerite ($Pb_5Sb_4S_{11}$). The intrusion contains two mineralization stages. The first stage is the mineralization of tin and the second stage is the mineralization of silver sulphosalt. The tin mineralization is located on top of the silver sulphosalt and is decreasing with depth. The Oruro massif consists of Tertiary igneous rock that has intruded into Palaeozoic metasedimentary bedrock (black slates). The intrusion dates back 16 Ma (Banks et al., 2002) and is represented by lavas, limonites, tuffs and aphanites (Patureau, 2007). These Tertiary igneous rocks are surrounded by Quaternary sediments and black slates from the Silurian-aged Uncía Formation (Banks et al., 2002).

Bedrock mega structures in the area have a northwest - southeast trend and are consistently faulted in the same direction (Appendix Fig. App. 1). The bedrock units in the area are part of the eastern margin of the central Altiplano. Four important formations are present adjacent the Challapampa aquifer, from oldest to youngest (i) the Llallagua Formation, (ii) the Uncía Formation, (iii) the Catavi Formation and (iv) the Vila Formation (Swedish Geological AB, 1992).

The Llallagua Formation was formed during the Silurian and is stratigraphically underlying the Uncía Formation. The Llallagua Formation is exposed around Oruro to a much lesser extent than the Uncía Formation, but follows the same megastructures as described for the area. The Llallagua Formation consists of sedimentary rocks; sandstone, siltstone and shale’s that vary from light grey and brown quartzite’s to greenish-grey sandstones. The Uncía formation is interpreted to be formed in the distal or middle part of the shelf and the transitional change from Llallagua formation to Uncía formation indicates a gradual change towards a less tectonic active basin. The Uncía Formation consist of grey to green shale’s with element of olive green sandstones and siltstones interbedded (Fig. 4) (Swedish Geological AB, 1992).

The Catavi Formation consists of sand- and mudstone that superimpose the Uncía Formation and is exposed in outcrops around the investigated area. In the northern extension of the Challapampa aquifer, and in alignment of the megastructures from Uncía Formation, the Catavi Formation is exposed but not the Uncía formation or any of the stratigraphically older formations. The Catavi Formation was deposited during the early Devonian in a proximal shelf and beach environment (Swedish Geological AB, 1992). The youngest Vila Vila formation was formed during the latter part of the Devonian and is exposed only in the northern part of the area. It consists of red-brownish saccharoidal sandstone, interpreted to have formed in a near shore environment.

It is expected to find ridges and topographical irregularities in the bedrock formations underneath the flat lying Quaternary strata on the altiplano north of Oruro (Banks et al., 2002). The northwest to southeast fault trend in the surrounding bedrock can be an expected feature in the buried bedrock as well as other features linked to the intrusions. The presence of hot springs in the eastern part of the area suggests a higher geothermal gradient in this part.

Fig. 4. In the outcrop east of the intrusion the bedrock consist of shale, micaceous limonitic sandstone and jarosite that has suffered propylitic hydrothermally altered to kaolinite. Photo by Måns Larsson.

3.2 Sedimentary geology

The Quaternary altiplano sediments have a varying thickness. Most of the sediments are deposited by fluvio-lacustrine processes, but also Pleistocene volcanic deposits are found within the area. The Quaternary sediments are most common and contain a significant groundwater resource (Banks et al., 2002; Dames and Moore, 1967).

Rigsby et al. (2015) performed eight drillings in a north-south transect between Lake Titicaca and Lake Poopó in the Desaguadero valley. However, none of them are located inside the study area, but irrespective of this of some interest. The drillings were limited to a depth of 50 m and thus only show the composition of the top part of the sediments on the altiplano. The three boreholes most relevant for this paper are those at Tejopa, Caquingora and Challacolla. Tejopa is located north of the investigated area and Challacolla south of it. Caquingora is located on the same latitude, but to the west of the area of investigation. The information retained from the eight drilling cores and down-hole logging with natural gamma radiation resulted in a differentiation with four facies associations. These four facies associations that form the subsurface strata of Rio Desaguadero are part of the hydrogeological drainage system between Lake Titicaca and Lake Poopó. The differentiated facies associations consist of (i) braided stream deposits, (ii) meandering stream deposits, (iii) lacustrine deposits and (iv) deltaic deposits (Rigsby et al., 2015). The meandering stream and lacustrine deposits (facies association's ii and iii) are present throughout the whole valley, while the braided stream deposits (i) are only present in two of the northern cores at Callapa and Zambrana. The deltaic deposits (iv) are only present in the southernmost core at Hauna Khaua (Rigsby et al., 2015).

The present study is focused on the flat-lying strata north of Oruro and will thereby not describe the braided stream deposits found in the northern cores, nor the deltaic deposit found in the most southern core, only the meandering stream and lacustrine deposits.

Characteristic of the meandering stream deposits in Rio Desaguadero is medium to coarse sand, fining-upwards into massive to planar laminated silts and muds, and with local concentrations of carbonate and/or evaporites. The lacustrine deposits are characterized by laminated to massive, variable coloured clay to clayey silt, with local concentration of carbon biological debris (Rigsby et al., 2015).

As described by Rigsby et al. (2015) the cause behind the sedimentation process for the deposited flat-lying strata of Desaguadero valley and Lake Titicaca is still under debate. Bills et al. (1994) present geophysical data that indicate a non-tectonically driven sedimentation of Quaternary strata during Holocene and late Pleistocene. Other authors (Baker et al., 2001a, 2001b; Fritz et al., 2004) suggest, based on drill cores and high lake-stands around Lake Titicaca, that during the last 50 000 years neither tectonic nor hydrological thresholds have changed the basin configuration.

Close (north) to the investigated area, close to the river Paria (Fig. 1), a few outcrops are exposed in conjunction with sand and gravel exploration. Here the sediments consist of sand to coarse gravel, but the top 30-50 cm consist of well sorted clay. In some outcrops there are distinctive layers of clay with high concentrations of salt present within deeper layers, but also big rip-up clasts of clay, and smaller lenses of sand and gravel, coated in clay (Fig. 5).

The surficial, fairly consistent and well sorted clay layer that is present all over the investigated area indicates that the latest depositional environment was a lake(s), while the well-rounded pebbles beds within the chaotic sediments below indicate fluvial transport. The size and concentration of the large pebbles suggest transport over shorter distances, probably from the surrounding mountains.

The investigated outcrops are located close to the interpreted discharge area of the Paria River and a reasonable conclusion is that the coarse-grained gravel content should decrease the further we move into the Challapampa aquifer. However, boreholes SELA and PP (Fig. 2 and Figs. 6-7) show the presence of gravel in the centre of the aquifer. From the drill protocols and exposed sediment sections it cannot be concluded the areal extension of the gravel deposits, but it is reasonable to assume that particle sizes are much smaller further down the alluvial fan at the drilling location, than shown in Fig. 5. The wide grain-size distribution, well rounded particles and particle orientation, as well as the lateral size of the exposed sections, suggest that the sediments within the investigated area have been transported under major but punctuated avalanche events, triggered by high energy water flows. This colluvium, shown in Fig. 5, is likely representing the upper part of an alluvial fan. The more distinct layers of clay were probably deposited during calm periods when the area was covered by lakes in between the high-energy flow periods and should be more frequent in the middle and lower fan segment.

The drilling technique used for the described boreholes was rotational drilling with mud-weighted drilling fluid. Such technique makes it hard to interpret the clay content from different layers. The concentration of different fractions is also hard to interpret purely from drill protocols chip analysis. The original drilling protocols are in the appendix section, Table. App. 1. However, the drill protocols indicate that parts of the alluvial fan deposits consist of well sorted sand and gravel and thinner sections with higher content of clay. All this is consistent with the expected deposits of a semi-arid alluvial fan. Alluvial fans are deposited by debris flow, sheet-flood deposits, stream flow and sieve deposits (Reading, 1986) and can extend hundreds of kilometres from the apex, normally in gradients between 3° and 6° (Reineck and Singh, 1975). Today the slope from the fan apex at Paria to Challapampita is less than 1°, and the top of the flat-lying strata over the investigated area has its origin in younger lake deposits superimposed on top of the alluvial fan. The exposed sections shown in Fig. 5 are interpreted as debris flow deposits and according to drill protocols the majority of the sediments within the study area are suggested to have the same properties as those exposed in the sections. Debris flow deposits are varying a lot depending on their source rock; when the weathered product of the source rock gives rise to high clay contents, it gives a fine-grained matrix that promote rapid flow velocities even at very low slope gradients. In Challapampa the investigated debris-flow deposits consist of sand as finest matrix fraction and large pebbles (<10 cm). The surrounding mountains around the Paria River consist of both shale and sandstone. However, investigated debris-flow deposits probably originate from sandstone beds as they lack the clay component (Reading, 1986). Further into mid-fan/fan-base positions are more fluvially-dominated deposits the norm. In the SELA drilling logs there are

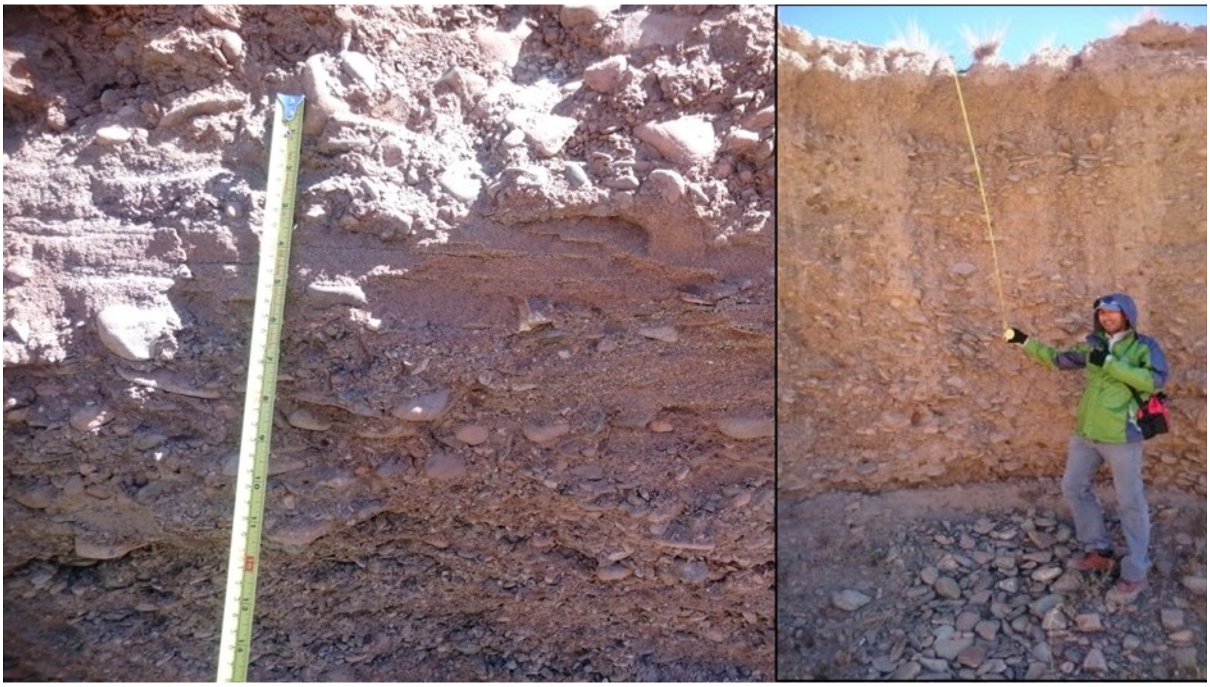

Fig. 5. Outcrops close to the Paria River. (A) Close up of the exposed sedimentary section north of the investigated area. (B)The exposed wall was around 4 m (Etzar Gomez poses as scale). Photo by Måns Larsson.

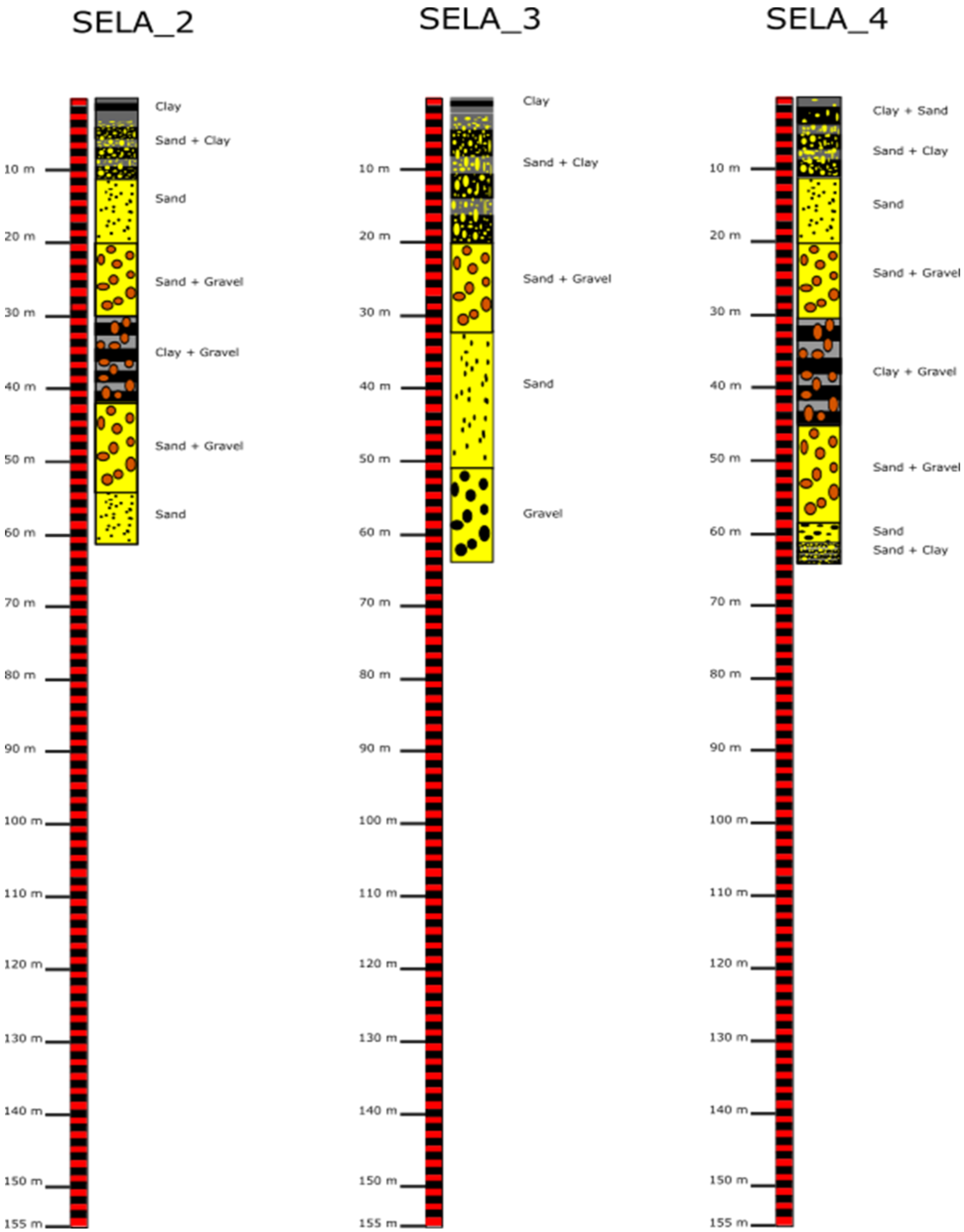

Fig. 6. Borehole logs for boreholes Sela_2, 3 and 4. Beds less than 2 m thick are generalised. The profiles are based on information retained from the consulting companies; Scide et al. (1981).

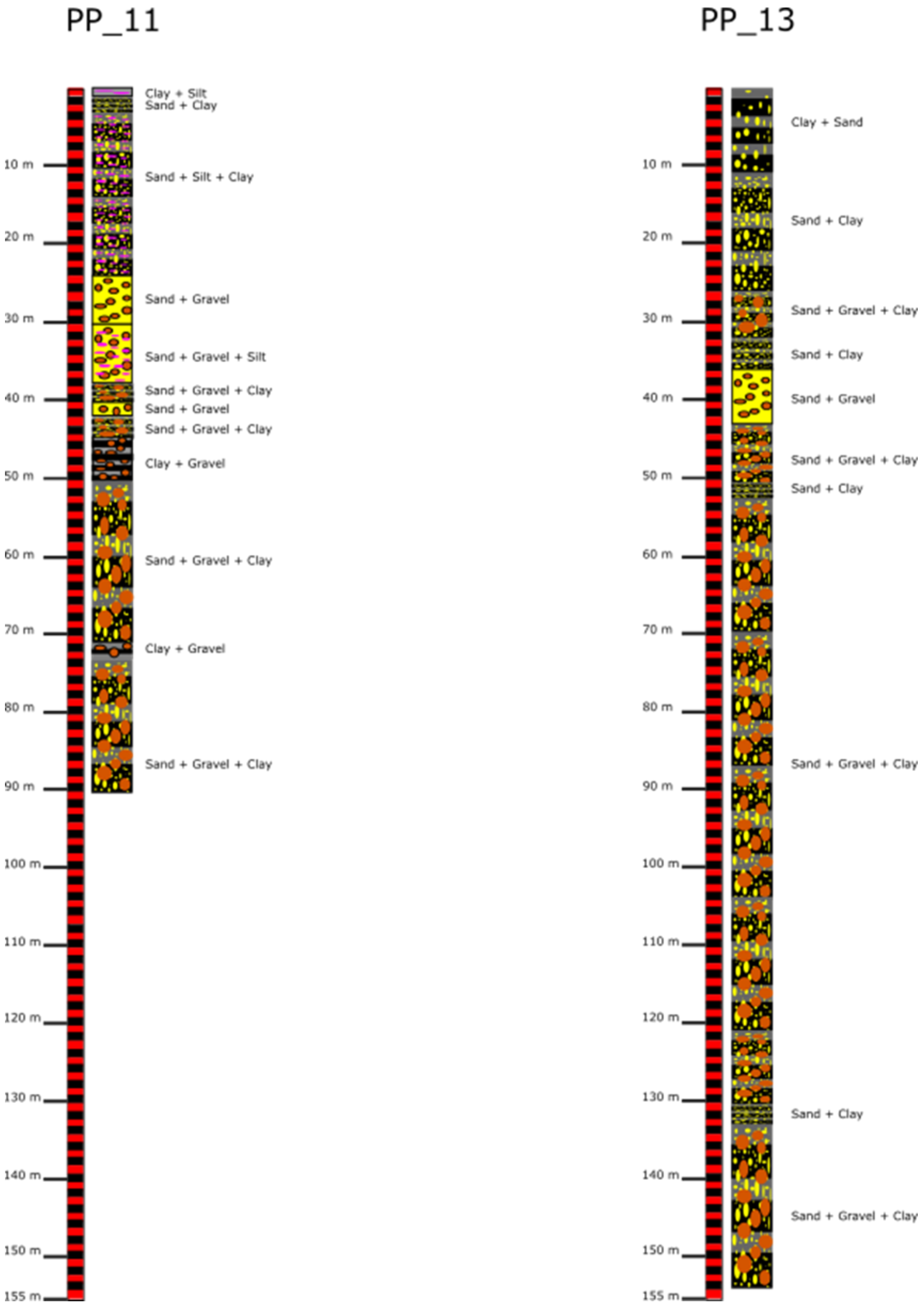

Fig. 7. Borehole logs for boreholes PP_11 and PP_13. Layers less than 1 m thick are generalised. The profiles are based on information retained from the consulting companies; Scide et al. (1981).

sections of well sorted sand and gravel that supports this assumption. To link this with one of the previous mentioned depositional environment is extremely hard as the drill protocols do not give any information about structures, sorting and the sections horizontal extent.

3.3 Hydrogeological features

The depth to the bedrock is in general closely linked to the hydrogeological flow trends, though the groundwater flow usually follows the topography of the bottom limitation of the aquifer. A contour map based on geophysical profiles and drilling logs has been produced by Dames & Moore (2000) and further developed by Banks et al. (2002). This map suggests that the basement of the aquifer is dipping towards northwest from Challapampita to Khala Kaja (Fig. 2). The general trend for the bedrock surface topography in the investigated area is that it is dipping towards west, with exposed outcrops to the east. There is a 150 m deep channel in the Khala Kaja area west of the investigation area, which is suggested to host the thickest sediment sequence in the area. At Challapampita the bedrock surface is at 100 m b.s. (meter below surface) (Banks et al., 2002). Swedish Geological AB produced in 1996 (Swedish Geological AB, 1996) a groundwater flow map based on the piezometric groundwater surfaces from wells in the area. This map suggest a general flow trend from northeast towards southwest, with an induced groundwater flow around the SELA well field with an approximate radius of 5 km. The groundwater flow seems thus not to follow the bedrock dipping trend between SELA and PP boreholes, which could be due to the locally induced flow towards the SELA well field.

The origin of the groundwater within the aquifer is debated by Gómez et al. (2016). Three sources for groundwater formation is presented based on isotope analyses and water conductivity; (i)the water tested in the central part of the aquifer at 40 m b.s. correspond with water from the Cayhuasi or Pongo Jahuira rivers, located significantly more north than the closest river Paria, the flows in these rivers are almost negligible during the dry season. (ii) The $\boxed{\delta^{18}O}$ values from the well field within the alluvial fan correspond better with those from the Paria river, which is more adjacent to the area and (iii), in the wells more southern position there are higher concentrations of evaporated minerals, which indicates a recharge source mostly from precipitation. These wells are not deeper than 100 m b.s.

Four different flow systems have been identified; (i) a shallow system characterized by high salinity with an electrical conductivity up to 0.1 S/m (10 ohm), reaching from ground surface and down to ca. 20 m b.s. This system is probably driven by precipitation during the wet season. The high evaporation during the dry season is increasing the salinity concentration in the top layers. The retention time for the water in the top layers are short and probably not more than one year old, though streams and ponds dry up fast during the dry season. (ii) Below this system is the next system, which is the target of most extraction wells. The conductivity ranges widely from 0.06 to 0.2 S/m (5 - 16.7 Ωm). This system reaches from 20 m b.s. until around 100 m b.s. This water is recharged by drainage from the surrounding mountains, the water transported to the alluvial fan with rivers. The main discharge area for this system is probably the well field. (iii) The third system is located underneath this and is a transitional system to a much older and deeper system. It is unclear if this system is located in sediments or bedrock, or both. No current wells are pumping below system number two, so there is no conductivity data from the deeper systems (iii and iv). (iv) The fourth and oldest system is characterized by the most depleted $\boxed{\delta^{18}O}$ isotopes. This indicates a recharge from high altitudes and/or from the latest palaeo-lake event. Groundwater in this system is suggested to flow through bedrock below 400 m b.s. (Gómez et al., 2016; Lizarazu et al., 1987).

3.4 Resistivity

Resistivity is a measurement of a material's capacity to resist conduction of electricity through it, and is defined as the potential drop (V) of the electricity when it passes through the material. The resistance (R) of the material is proportional to the length (L) of the electricity passage and inversely proportional to the cross-section area (A). When more than one medium is present both medias geometry and electrical properties becomes important and also the direction of measurement. Layered models can have different resistivities depending on what direction the measurement is made (anisotropy). Electricity passage following the orientation of clay particles will, e.g., give much lower resistivity than if the measurement is made 90° degrees to their orientation. Measurements will include all heterogeneities within a sediment/rock unit and the resulting resistivity will be an average value of all variations within the material (apparent resistivity). Resistivity is measured in ohm-meters (Ωm) and its inverse, conductivity, is measured in Siemens/meter (S/m). Usually it is resistivity that is measured during geophysical investigations, but in high-current densities it can be more suitable to use conductivity (Reynolds, 2011).

The measured resistivity from the subsurface will vary with many involved factors. The most important parameter that affects the resistivity is the presence of water in the pore spaces and/or fractures of rock or sediment, this since air has high resistivity and water have relative low resistivity. There is a range of factors that affects the mean resistivity for a subsurface layer. In a dry medium the relation of air and interconnection between grains and their mineralogy are the most decisive factors of resistivity. Grain to grain relationship in unconsolidated sediments depends on the grain size distribution and clay content. A well sorted sediment has a higher porosity than a poorly sorted sediment. Clay particles are flat and can have a much higher grain to grain contact during the same porosity as bigger sized particles, and thereby lower resistivity. The general rules are that the resistivity is decreasing with increasing clay content, pore water and salt concentration. Crystalline non-fractured bedrock has higher resistivity since it cannot contain as much water. Temperature is also a factor that affects the resistivity. The resistivity is decreasing with increasing temperatures at a constant salinity until 300℃ (University of Alberta, 2014). All standardisations mentioned above are much generalized and there are a lot of different circumstances that can change the formations apparent resistivity. Bedrock with very high concentrations of conductive minerals can for example have a significant lower resistivity than wet sediments or even the same resistivity. These circumstances are called the equivalence problem. There are a number of different geological formations that might have the same resistivity response, as illustrated in Fig. 8. A summary of resistivity values for pure sediments and bedrocks that are relevant for this specific area are presented in Table 1. If there is significant pore space in the sediment and if it is water saturated, then the chemistry of the pore water is highly affecting the sediment resistivity. Fresh water has a higher resistivity than salt water; thus the resistivity is decreasing with increasing salt content. In salt water there are more free ions available that can carry the electrical current. If the pore water is salty, the resistivity of the mineral grains is almost always higher than for the salty pore water (University of Alberta, 2014). When this is the case, Archie's Law can be used saying that $\boxed{\rho = a\varphi^{-m}s^{-n}\rho_w}$. The equation describes the effective resistivity ($\boxed{\rho}$) of a formation and considers the formations porosity (**φ**), how much of the pores that are filled with water (s) and the resistivity of the pore water ($\boxed{\rho_w}$), while "a", "m" and "n" are constants (Reynolds, 2011).

4 Method

The Challapampa aquifer was mapped using the Transient Electromagnetic Method (TEM). TEM is a geophysical technique that uses transient electromagnetic (EM) waves to penetrate the ground. The method is point based, meaning that different investigation designs can be used for different purposes. In general the

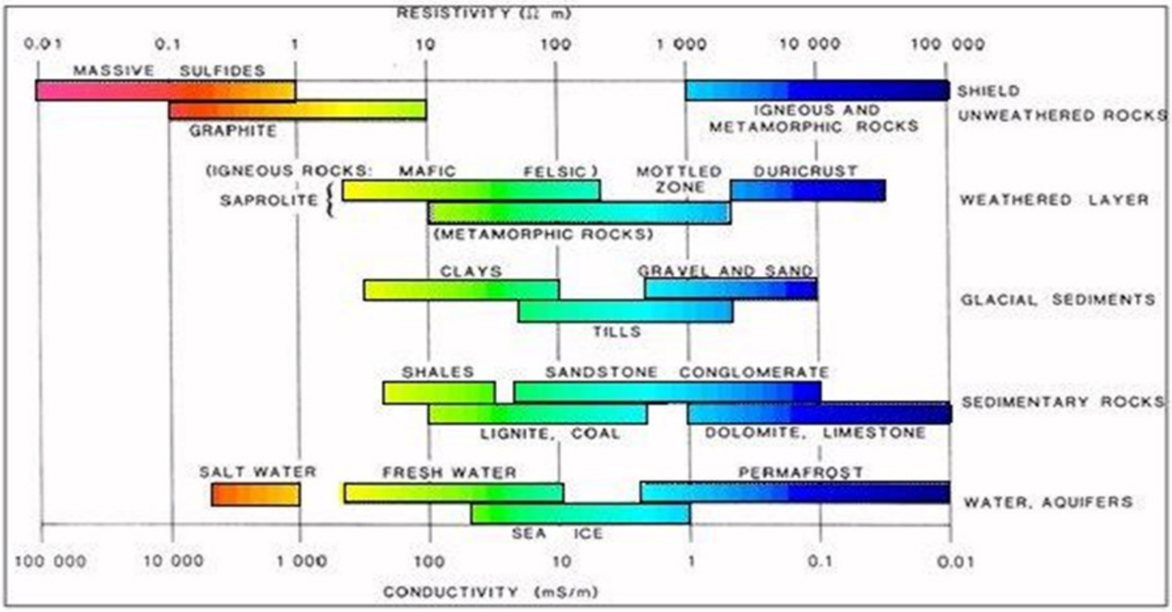

Fig. 8. Resistivity and conductivity ranges for different geological materials. A number of different materials might show overlapping resistivity. Figure taken from Palacky (1987).

Table 1. Resistivity values of different geologic materials. From Reynolds (2011).

Material	Resistivity Ωm
Gravel (dry)	1400
Gravel (saturated)	100
Quaternary sand	50 - 100
Sand (dry)	80 - 1050
Clay	1-100
Clayey sand	30 - 215
Sand and gravel	30 – 225
Slates	600 - 4 $* 10^7$
Conglomerates	$2 * 10^3 - 10^4$
Sandstone	$1 - 7.4 * 10^8$
Limestone	$50 - 10^7$

method has a high depth penetration with good resolution, but is varying a lot with different geologies. It is thus well suited to find and map low resistivity layers (Reynolds, 2011).

The first electromagnetic method was developed by Karl Sundberg in Sweden (Sundberg, 1931) for mineral exploration. But the electromagnetic methods did not take off until mid-1960s; since then it has gotten a wide range of applications, e.g. from petroleum and mineral exploration to environmental applications (Reynolds, 2011). The TEM method has mostly been developed during mid 1980s and it is thereby a young method in the context. This "hold back" is due to two main problems that had to be solved: (i) the response signal covers a wide dynamic range so highly advanced electronics are required and (ii) interpreting TEM data requires a lot of computing power which has not been available earlier (Christiansen et al., 2009).

4.1 Theory

The TEM method is based on Maxwell equations that describe the behaviour of electromagnetic waves. A magnetic field is created by an electrical current passing through an ungrounded cable. When the current is cut off, as quickly as possible, the magnetic field induces a current in its surrounding ground that results in a secondary magnetic field. The strength of the field and induced current will vary depending on the strength of the primary field and the resistivity properties of the conductors. The secondary magnetic field induces a current in the receiver antenna and electrical potentials are measured and registered in the instrument.

Magnetic fields change over time by growth in size and decrease in strength the longer from its source (Nabighian and Macnae, 1991). Getting information about the subsurface is based on the differences in phase and amplitude of the secondary field compared to the primary field, which is a result of different resistivity in the subsurface. The resistivity in the subsurface changes according to electrical properties of earth materials, geometry, size, porosity, pore fluids, etc., and results in different strength on eddy currents (Christiansen et al., 2009; Reynolds, 2011; Loke, 2013). The instrument measures the induced electricity in the receiver coils that is proportional to the secondary magnetic field (B) over time (dB/dt). A recalculation is then transforming dB/dt to apparent resistivity (roh_a). Apparent resistivity is the mean resistivity over the area influenced by the magnetic field. Only when applied in a complete homogenous medium the apparent resistivity is equal to the real resistivity (Christiansen et al., 2009; Loke, 2013).

The area that is influence by the magnetic field is increasing with depth and, as a result, there are higher uncertainties linked to apparent resistivity on the deeper layers. Configuration of the TEM setup also affects the magnitude of apparent resistivity. More about this is described in the practical section of the methods chapter.

TEM is a time-domain method that measures the amplitude of a signal as a function of time in logarithmic time gates. This gives an indirect measurement on the secondary field. To accomplish this, short pulses are used to create the primary magnetic field (Fitterman and Stewart, 1986). By sending electrical pulses, a static magnetic field proportional to the current is created. When a pulse stops the primary magnetic field disappears, leaving eddy currents that propagate down in the subsurface. This is due to electromotive forces emitting secondary magnetic fields according to Faraday´s law (Fig. 9b)(Reynolds, 2011). At the same moment the primary field shuts down, the secondary field intensity is equal to the primary field. The secondary magnetic field is indirectly measured through a receiver coil that is induced with electricity (Fig. 9c). This field is normally measured 0.00001 s after the current is turned off until 0.001 s. The early stage of the measured signal will be much stronger than the late stage. The time window that register the signal, called a gate, increases logarithmically in time to compensate for background noise of the late weaker signal. The measurement needs to be in an interval long enough to give the amplitude of the signal a dynamic range or variation factor to around 1 000 000. During one measurement the pulse is normally turned on and off 1 000-10 000 times and an average for each gate is calculated, called stacking, to increase the signal to noise ratio (S/N). The electrical pulse consists of different phases; the turn on ramp starts when the first electricity enters the loop and stops when the desired current is reached, which this takes about 1-30 µs. The on time for one pulse is 1-40 ms and is followed by a 1-40 ms off time when the measurement is made (Fig. 9a) (Christiansen et al., 2009). After every pulse the next one is sent in the opposite direction (negative).

The first current passes through the loop in a clock-

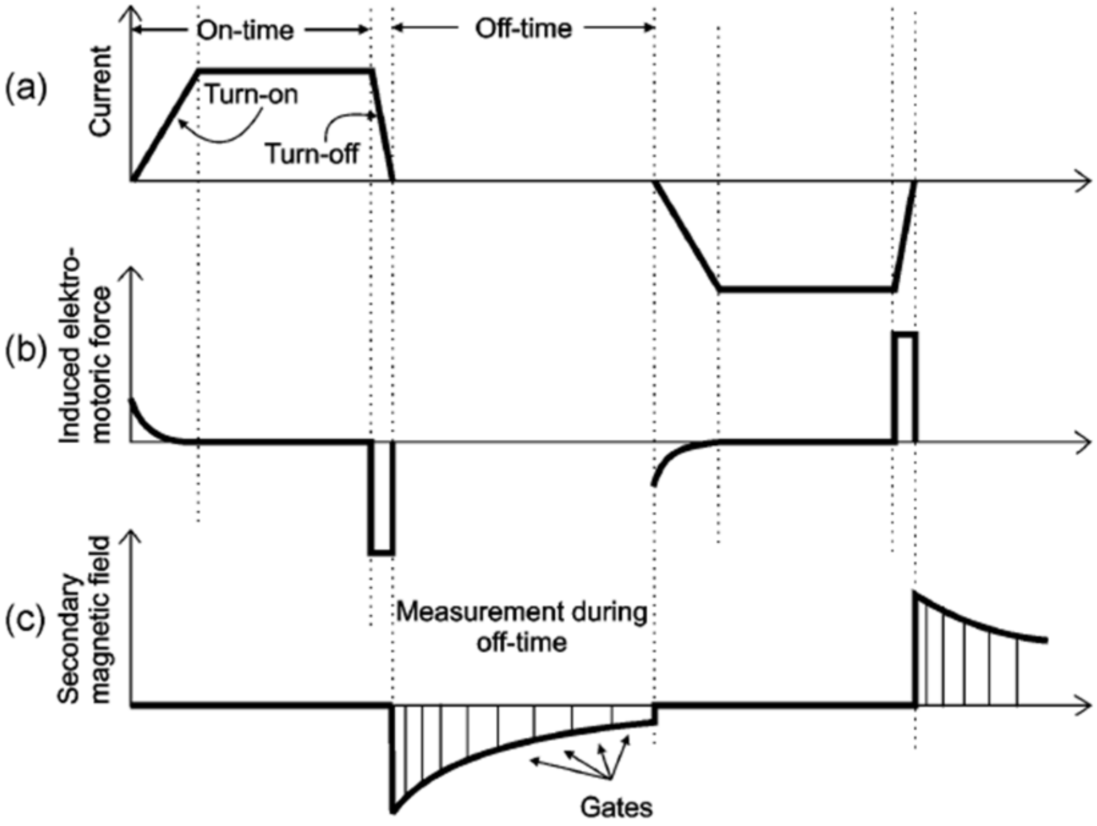

Fig. 9. The figure demonstrates what happens during a pulse event in a TEM instrument. (a) The different stages in a turn-on and off cycle. (b) The electromotive force that propagate downwards in the ground during the turn off. (c) The gates where the secondary magnetic fields are registered in logarithmic scaled gates. From Christiansen et al., 2009.

wise direction, based on the “right hand rule”, which gives a magnetic field that propagate down in the ground inside the loop (Reynolds, 2011), but as earlier stated the pulses change direction after every turn off and so will the resulting magnetic fields.

The S/N ratio follows a proportion to $\sqrt{N}$ (N= number of measurements in a stack), which means doubling the stacking in logarithmic gates leads to an improvement of the S/N by 1.41. Stacking helps delaying the signal from drowning in noise by elevating it on the dB/dt graph (ads shown in Fig. 10). Since the measurements cover a wide range of amplitudes the method is sensitive to natural background noise as, e.g., lightning, radio and radar signals (McNeil 1994). In the top layers it is easy to distinguish signals from noise, but in the deeper layers when the signal has been decreasing it is harder, and the depth penetration of the measurement thus depends on when the signal “drowns” in noise. The natural background noise normally follows the trend $t^{-1/2}$, while the earth´s natural response normally follows the trend $t^{-5/2}$. When the latter crosses the noise the transition from good S/N to bad S/N happens (Fig. 10). More direct noise is emitted from power lines, which can be corrected for by stacking though the frequency is often known (50 Hz in Bolivia). Increasing the depth of penetration is a matter of being able to distinguish the late signal, which can be done, as previously mentioned, by stacking that will prolong the transmitting time and increase the initial signal strength (Christiansen et al., 2009).

Apart from natural background noise other disturbances might affect the measurements significantly. It is important to keep at least 100 m distance from man-made constructions that involve laterally extensive conductors such as pipes, cables, railroads and fences. Constructions like these are very conductive and if they are within the primary magnetic field they will emit false signals not representing the ground properties. The signal emitted from these have the same delay time as the signal from conductors in the ground

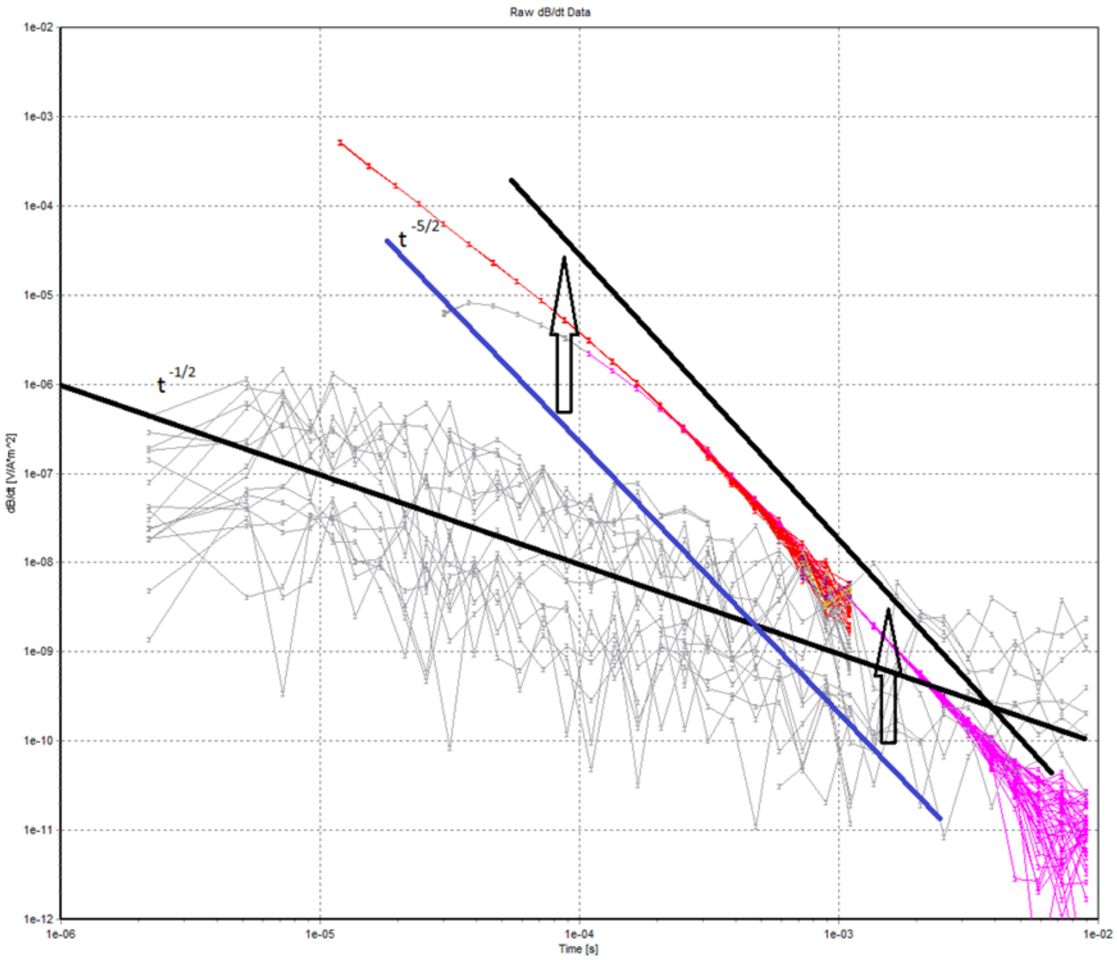

Fig. 10. Station 97, showing the general trend of the natural noise $t^{-1/2}$ and the trend of earth response $t^{-5/2}$ The solid black $t^{-5/2}$ line indicates the effect of stacking, delaying or raising earth's natural response line out of the noise.

and cannot be sorted out in the data (further described in the Magnetic field section).

During the turn off, an electromotive force is sent downward close to the speed of light (as illustrated in Fig. 11). This force is measured in current density and propagates down asymptotically along a cone with a 30° angle to the horizontal plane. The horizontal area affected is thereby growing by a factor of 2 for every unit of depth of penetration. The lateral extent covered by the magnetic field in the ground will thereby be much greater with depth, which will affect the apparent resistivity. Over time, the horizontal spread will be twice the vertical spread, creating a smoke ring like pattern. In reality these smoke rings spread almost instantly but are only shown on greater depth after time has passed since the signals are many magnitudes lower at 1 000 µs than at 10 µs. Every smoke ring causes continuously secondary magnetic fields containing information about that depth.

Introducing a layered model to this concept with a top layer of higher resistivity followed by a low resistivity layer and then a new high resistivity layer in bottom, makes the smoke rings behave differently. In the top layer the current density behaves as normal but when the current density enters the low-resistivity layer, it is easier for the current to travel within this layer instead of propagating down in the higher-resistivity layer. The effect of this will be that the lower high-resistivity layer will be hidden, emitting no or a very weak secondary magnetic field (Fig. 12). Since the bottom limitation of the low-resistivity layer can be located, an indirect assumption of where the top of the high-resistivity layer is located can be made (Christiansen et al., 2009).

4.2 Magnetic fields

Under the theory section in the method chapter it is stated that the primary magnetic field is varying in strength according to Faraday's Law depending on the induced voltage. There is a lag between the primary magnetic field and the secondarily induced electricity. This means that the secondarily induced electricity will be zero in amplitude when the primary magnetic field is at its maximum or minimum. This phase lag is defined as π/2. The eddy currents that create the secondary magnetic fields are created from the induced volt-

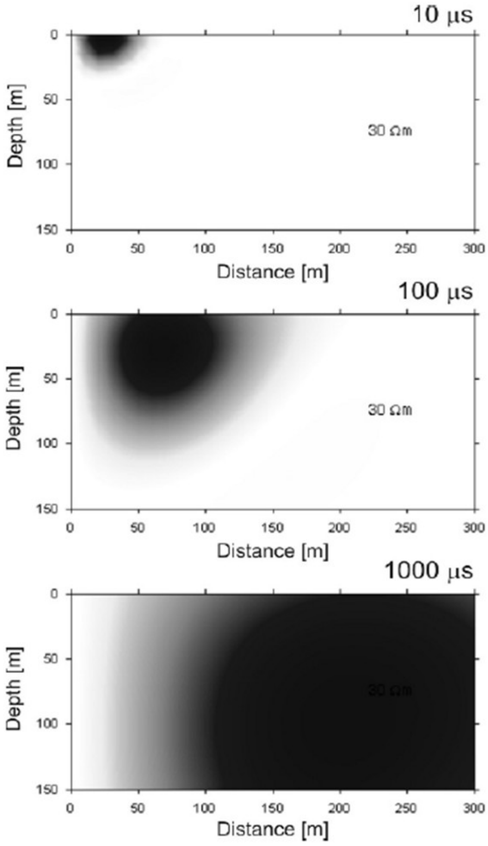

Fig. 11. Current density as a response of a pulse in a resistivity-homogeneous material. Note that this is the current density maximum and not absolute values where the maximum is several magnitudes lower in the 1000 µs than in the 10 µs. From Christiansen et al.,

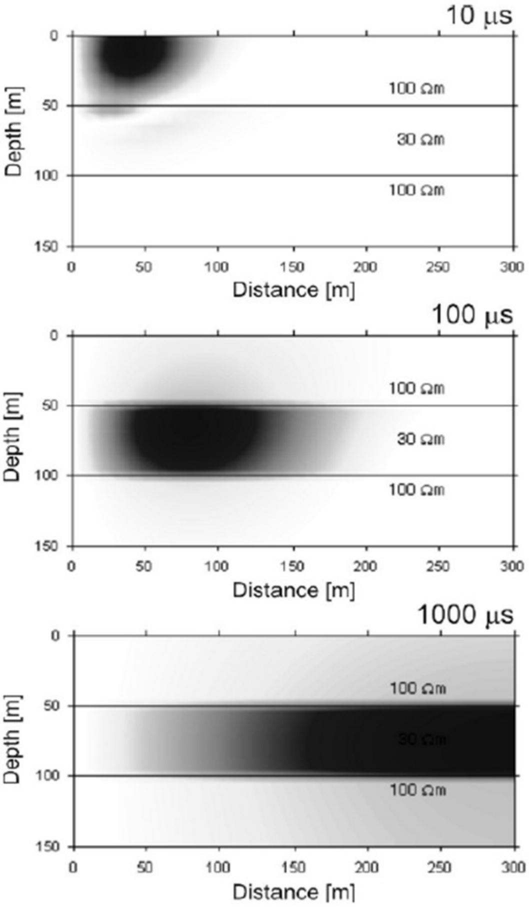

Fig. 12. Current density distribution in a layered model. The low resistivity layer "consumes" the current, blocking the higher resistivity layer beneath it. From Christiansen et al. (2009).

age over finite time, defined as (α=tan-1L/R), varies with the electrical properties of the material. Good conductors result in low amplitude fields with slower decay process and bad conductors result in large amplitude fields and a faster decay process (McNeil, 1980). Since the instrument only records induced electricity in the receivers there is an additional lag of one π/2, giving the total lag time between the primary magnetic field and the resulting induced electricity in the receivers to 2(π/2)+ α. This lag makes it possible to indirectly measure the secondary magnetic fields without the primary magnetic field present (Reynolds, 2011; Beck, 1981).

Assuming that the primary electrical pulse is sent in a clockwise direction it will create a primary field propagating up in the centre of the transmitter loop (Fig. 13). The resulting secondary field will thereby propagate up through the centre loop but down through the offset loop, giving negative Values. On deeper levels the primary field has not only propagated down but also out, when it passes the RC-200 receiver in the lateral direction the secondary magnetic field will change from propagating down in the RC-200 to up, as illustrated in fig. 13. In the data set this can be detected in the LM (low moment) data from the RC-200, where the measured data peaks and changes direction. In the HM (high moment) data this is not detectable, because it happens in the early gates. In the RC-5 the magnetic field do not change direction, though it is located inside the transmitter loop. This makes the RC-200 more sensitive to correct placement than the RC-5 receiver.

4.3 Inversion

When inverting the acquired data the aim is to find a model that fits the measured data as good as possible. The created model is a mathematical representation of the measured data, including model parameters. The model parameters vary and makes sure that the model is realistic and, if possible, supported by additional reliable information. From the created model, includ-

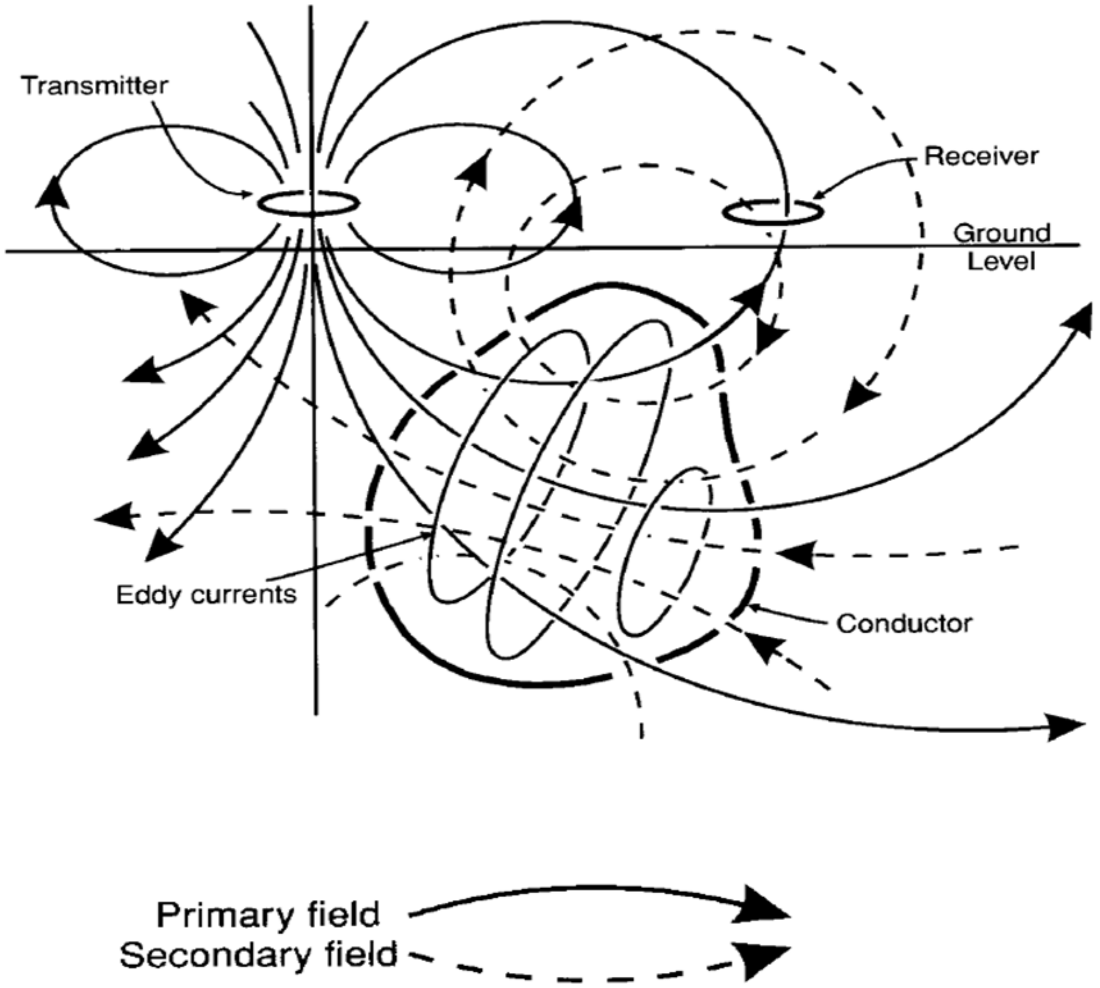

Fig. 13. Illustration of primary fields and resulting secondary fields. From Grant and West, 1965.

ing model parameters, synthetic data can be calculated (model response). The model response should be as similar to the measured data as possible, this to represent the subsurface as closely as possible (Loke, 2013). Inversion theory uses measured result to estimate the causes or model parameters which created the result (Fig. 14). Forward theory is the opposite of this; in such the model parameters are known or observed and used to calculate a prediction of the results (Fig. 14) (Menke, 1989). It is possible to create an infinite number of models that fit the data and it is thus important to have complementary information in order to be able to select the most applicable model(s). As an example, this can be carried out within an expected model that is created based on available archive information prior to the investigation. The inversion can then be used to refine or reject the expected model.

In geophysical investigations inversion theory is the norm, since the model parameters often are unknown. Model parameters in TEM investigations include depth to layers, layer boundaries and resistivity values for the layer(s). Every parameter that affects the physical properties of the subsurface is a model parameter (Parker, 1994).

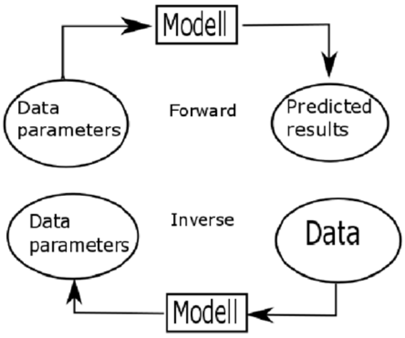

Fig. 14. Forward theory vs. inverse theory. From Måns Larsson

4.4 Data acquisition

There are different setups of the TEM instrument depending on what the target is for the investigation. Normally a centre loop configuration is used with a 40x40 m cable as a transmitter and the receiver placed in the middle. Different sizes on the receiver and transmitter can be used to get better resolution from deeper layers, but also different setups of the instrument.

In this project a 50x50 m AWG 12 cable was used as a transmitter loop, together with two receiver coils, one at 0.59x0.59 m (RC-5) and the other at 10x10 m (RC-200). The instrument WalkTEM by ABEM was connected in series with two 12 V car batteries, which produced a current in the transmitter of around 20 amps during high moment and 2 amps during low moment. This is specific to our setup and can be varied for other purposes.

The RC-5 was placed in the middle and RC200 with and offset of 50 m from the centre of the transmitter loop. When two receiver coils are used the RC-5 is used in a central loop configuration and will only use data from LM, while the RC-200 is only using HM.

A field guide was produced prior to the campaign. A short version of it is summarized below:

Setting up the instrument with a 50 m x 50 m transmitter loop

1. It is imperative to have a measuring plan with exact coordinates for the centre of the layout. Place the RC-5 receiver antenna on the premarked coordinate. A minimum distance of at least 100 meters to existing conductive installations such as pipes, vehicles, metallic cases or reels is recommended.
2. Use a rope to mark the corners of the transmitter loop, with a distance of 35.71 meters from the far corner of the RC-5 receiver antenna. Start in a predefined corner and unroll the transmitter cable clockwise.
3. From the instrument corner, follow the transmitter cable to a 20 m mark and at this mark use a 20 rope to mark the RC-200 connector corner. The three remaining corners on the RC-200 should be marked. Make sure that both corners closest to the transmitter cable are at a distance of 20 m. Stretch the sides and fix the remaining 2 corners.
4. When all loops are in place, make sure that the RC-5 connection cable crosses the transmitter cable in a 90 degree angle to minimize interference. Connect the RC-5 to input A, and the RC-200 antenna to input B.
5. The instrument should be connected to an external power source before starting the instrument. A three meter long cable should be used to connect the transmitter loop and be connected with a damping resistor.
6. Start the instrument and run a measurement. If all the loops are connected clockwise a positive signal is registered and shown as red markings in the dB/dt-graph, while a blue marking indicates a negative signal.

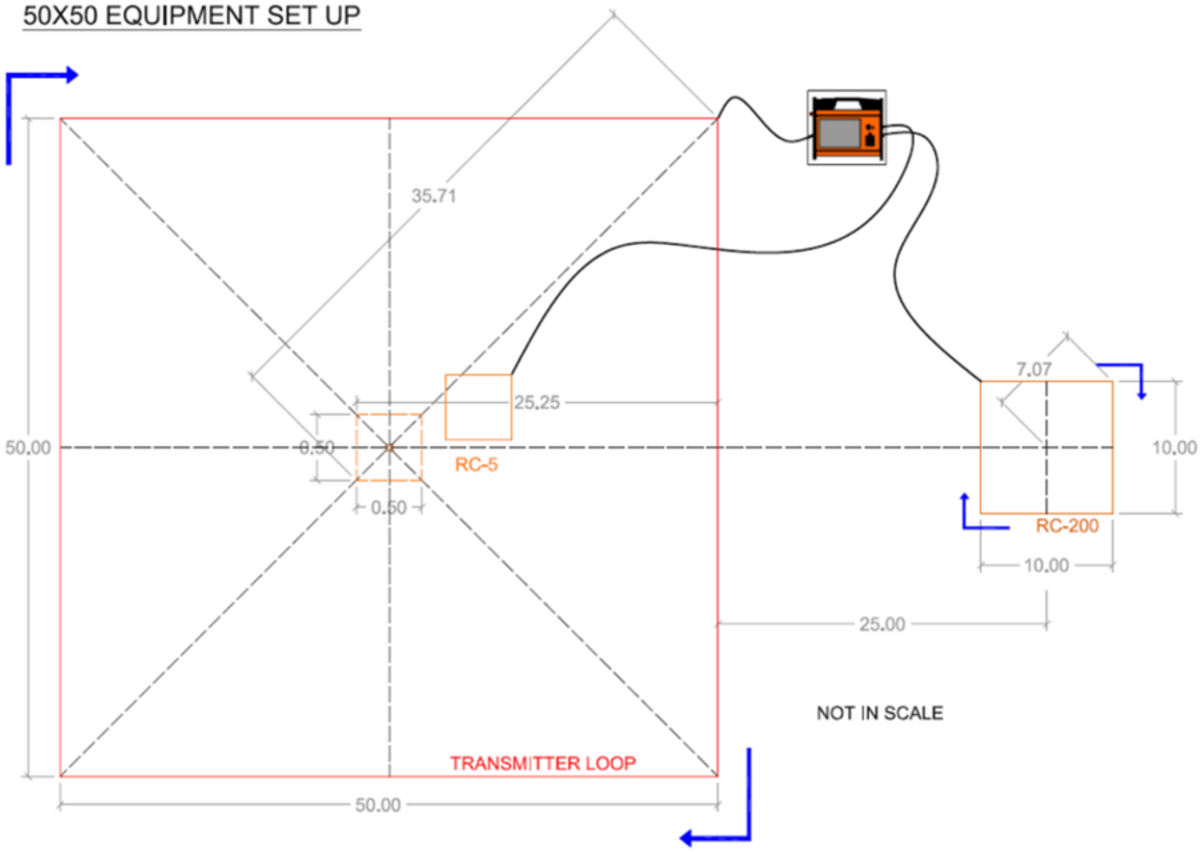

4.5 Data processing and inversion

At the post-data gathering and evaluation process a sorting of outliers and editing of the channels from the different receivers are made. This is done in the inversion program ViewTEM, the same program which runs the numerical inversions on every measurement. The arrangement is a 50x50 m central loop configuration with the RC-200 receiver placed as offset 50 m outside the transmitter loop. Channel 2 (CH2) records high moment for RC-5 and channel 3 (CH3) records low moment for RC-200, both of these channels are disabled. The HM pulse (CH2) will saturate the RC-5 amplifiers due to the high induced voltage from the turn off of the primary field. It is technically difficult to turn off the current instantly, so after the turn off, smaller amounts of current “leaks” to the surrounding, adding to earth´s natural response giving away false readings (Christiansen et al., 2009). Channel 3 was not used since the RC-5 has an improved resolution for the top layers. The early data points in channel 1 (low moment for RC-5, CH1) was disabled as well since the focus of this investigation is to detect the bedrock position at deeper depths. Early data points in CH1 can be disabled to get a better fit of the deeper layers and also to avoid ringing effects if the damping resistor is not working perfectly.

When all data are processed, the ViewTEM program runs an inversion algorithm creating a model that fits within the error bars of every measurement point. In practice there are no measurements that are noise free, which means that all measurement points are assigned an error bar. This results in an infinite number of models that can fit the data. If the error bars are small, most of the models that fit the data will be very similar and thereby more probable. Different model parameters can be determined by fixing; thickness, depth, and or resistivity of the layers. A good fit of the model with as few layers as possible, called a layered model, indicate a higher probability that the mean resistivity within a specific layer is correct. The smooth models have the specification of always using 20 layers with increasing thickness with depth. It is preferable to detect smaller and more gradual resistivity transitions with the smooth model. However, big jumps in resistivity, e.g. sharp transitions, will still be displayed as a more gradually transition and thereby not true.

When visualizing the data a program called Aarhus Workbench was used. Workbench can be used for visualization of geophysical data from several different techniques, but can also run inversion. In this study Workbench has only been used for visualization of the TEM-data in horizontal maps on different depths and also to produce profiles with interpolation between the measured data points. A selection of maps and profiles are presented under the result chapter and all maps and profiles produced are presented in the appendix Fig. App 2-8.

5 Results

As results for the investigation a selection of three profiles and six horizontal maps have been produced to visualize the resistivity range at different depths over the investigated area. The profiles and the location of the two correlation points are marked in Fig. 15. The program used to visualize this is Aarhus Workbench, developed by the Hydrogeophysics Group from Aarhus University.

The horizontal visualizations of the results present resistivity values for different depths of all the measurements made in the area. The color scale in Fig. 16-24. is logarithmic with dark blue indicating the lowest value (1 Ωm) and bright purple indicating the maximum value (1000 Ωm). The maps present the mean resistivity value over the thickness of a chosen interval. The top 20 m b.s. have been visualized with a 2 m thick intervals based on the layered model to make the transition from the top dry sediments to saturated sediments as visual as possible. After constructing the 20 m b.s. maps, the others are produced with 10 m thick intervals down to a depth of 300 m b.s. At this depth significant gaps in the data appear. The deepest measurements extend to 850 m b.s. All produced maps are presented under the appendix section, Fig. App. 2-5.

The general trend is that the resistivity values are lower in the top layers and are increasing with depth. The east parts of the survey area have lower values than to the west for the top 2 m b.s.

In the eastern part of the investigated area, adjacent to the hot springs, the groundwater surface is situated directly underneath the surface and is highly saline. This represent the lowest resistivity values around 2 Ω m (Fig. 16). Two correlation points located remotely northwest and east of the studied area are situated directly on top of bedrock with resistivity values around 25 Ωm in the surface (Fig. 15).

Changes in resistivity, mainly in the western part of the area, to around 10 Ωm in the 10-12 m b.s. interval is interpreted as the depth at which the sediments

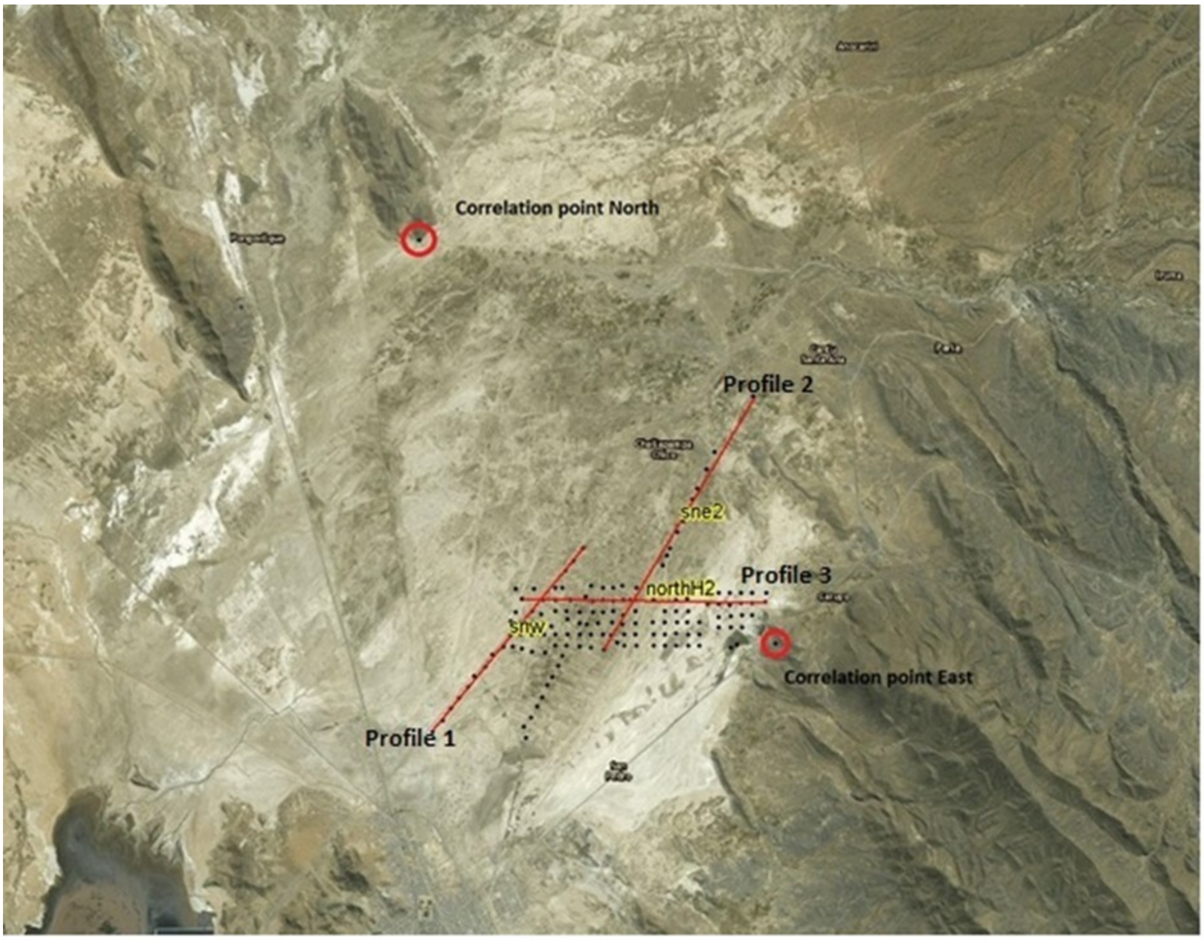

Fig. 15. The presented profiles within the investigated area and the two correlation points marked.

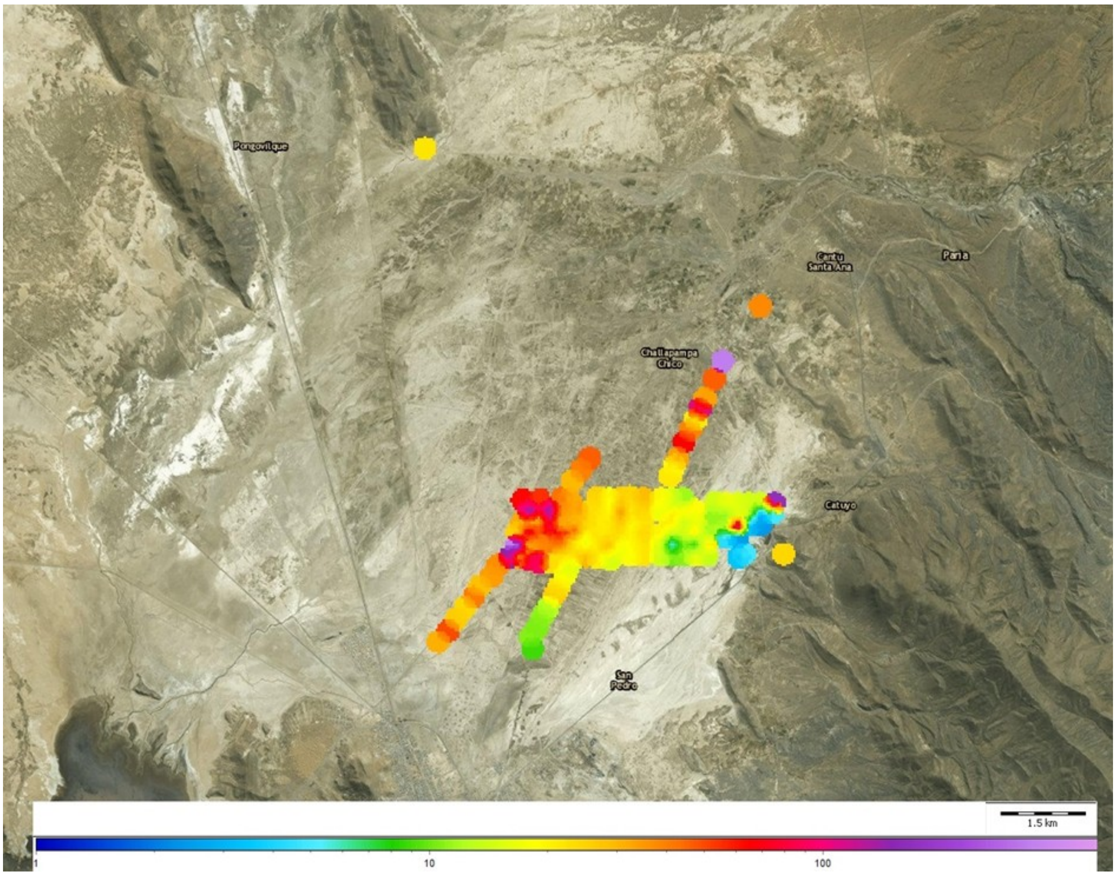

Fig. 16. Mean resistivity values for the interval 0-2 m b.s.

become fully saturated (Fig. 17). The eastern part still shows low resistivity values for this level, around 2 Ω m, indicating the highly saline water that is present on the surface for this part of the area. In between the eastern and western parts, the resistivities range from 8 -30 Ωm.

The next tangible change in the horizontal maps is in the interval 60-70 m b.s. (Fig. 18). Higher resistivity values are distinct along the Sne2 profile, as well as in the southwest part of the area, at around 100 Ωm. A first indication of resistivity values around 200 Ωm can be detected where the southern right line meets the grid. Lower resistivity valleys (8-20 Ωm) are shown in a northwest to southeast direction in the central and eastern part of the area. Both correlation points show increased resistivity values, mostly the eastern point that is around 200 Ωm at this depth, while the northern point is around 100 Ωm.

The interval between 120-130 m b.s. still shows lower resistivity values for the western valley, but higher than previous interval, now between 20-40 Ωm (Fig. 19). There are continuous low resistivity values for the eastern valley between 8-20 Ωm. Likewise, higher resistivity values for the western part of the area are expanding with depth. The high resistivity values occurring where the southern east profile meets the grid show increased resistivity to around 1000 Ωm. The northern correlation point has the same resistivity as in the previous map (100 Ωm), while the eastern point have decreased its resistivity to 30 Ωm from previously 200 Ωm. Some of the sounding points have no resistivity data from this depth and downwards because of a limited DOI (depth of investigation). As a result the first gaps in the grid appear.

At the interval between 170-180 m b.s. a clearer high resistivity ridge appears in the western part of the area (Fig. 20). The resistivity of this ridge is between 200-1000 Ωm and trends southwest to northeast direction, i.e. in the same direction as the low resistivity valleys. There is still a small indication of the western low resistivity valley, while the eastern low resistivity valley is still very clear. The correlation points are similar as in previous map, 100 Ωm in the northern point and 30 Ωm in the eastern point.

The deepest interpreted map is in the interval between 280-300 m b.s. The deeper maps are characterized by gaps in the data grid. For Fig. 21, high resistivity values mark the general trend of this map. The low resistivity values are representing the east part of the area with values as low as 5 Ωm. The general trend shows decreasing resistivity values towards east until the hot springs, while the high resistivity ridge in the western part is more coherent. The eastern correlation point shows increased resistivity to from 30 Ωm to around 100 Ωm over this depth interval, while the northern correlation point remains unchanged at 100 Ωm.

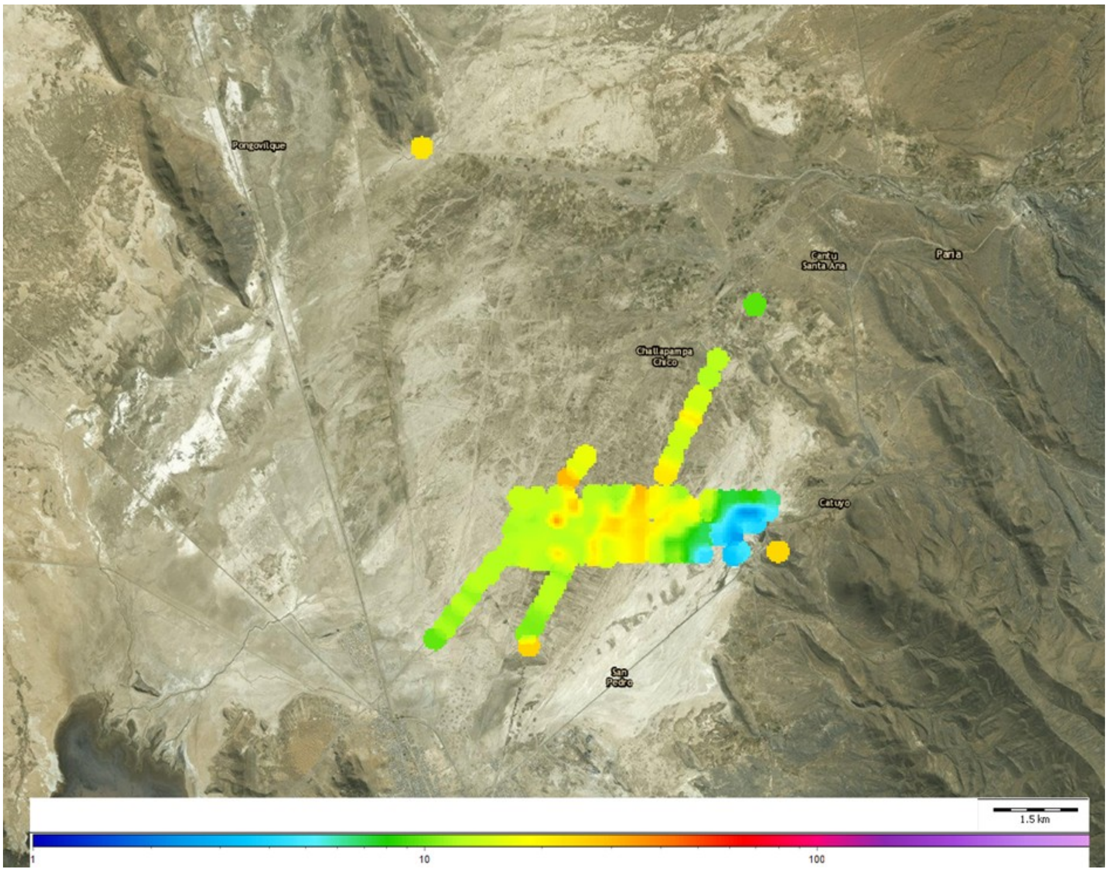

Fig. 17. Mean resistivity values for the interval 10-12 m b.s.

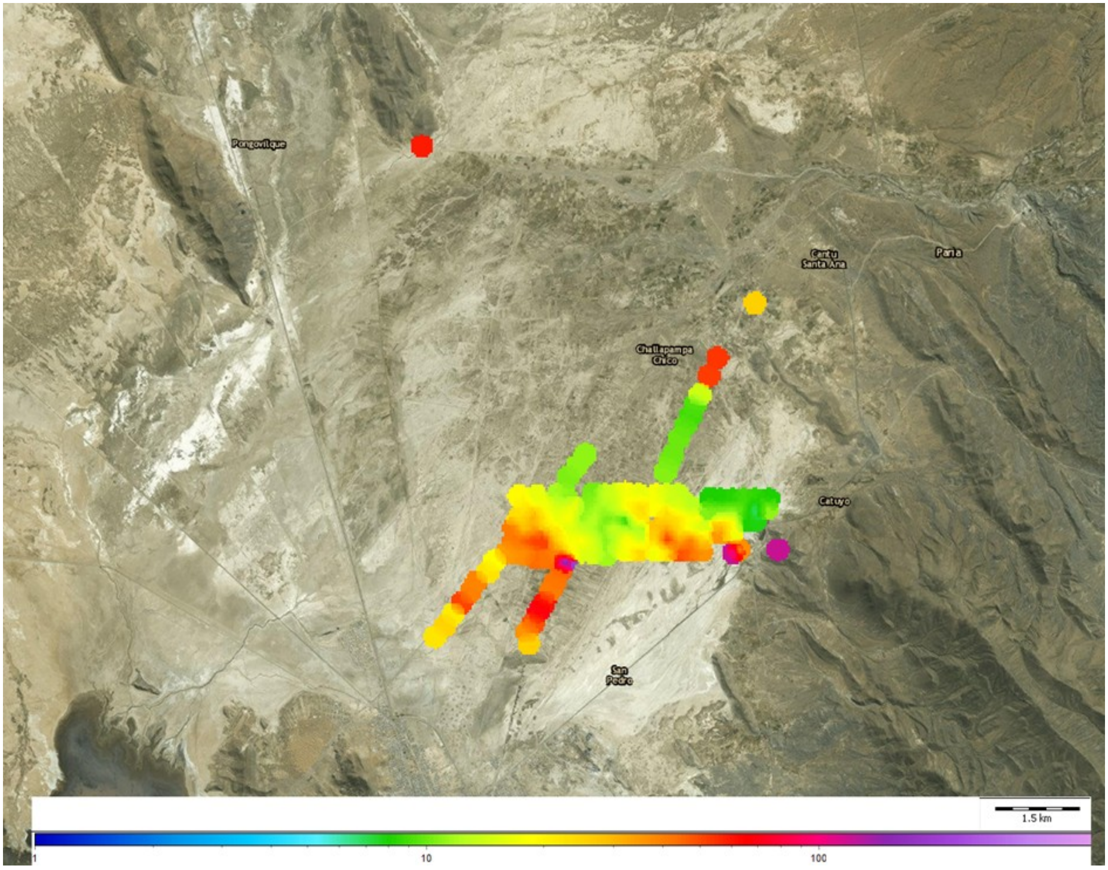

Fig. 18. Mean resistivity values for the interval 60-70 m b.s.

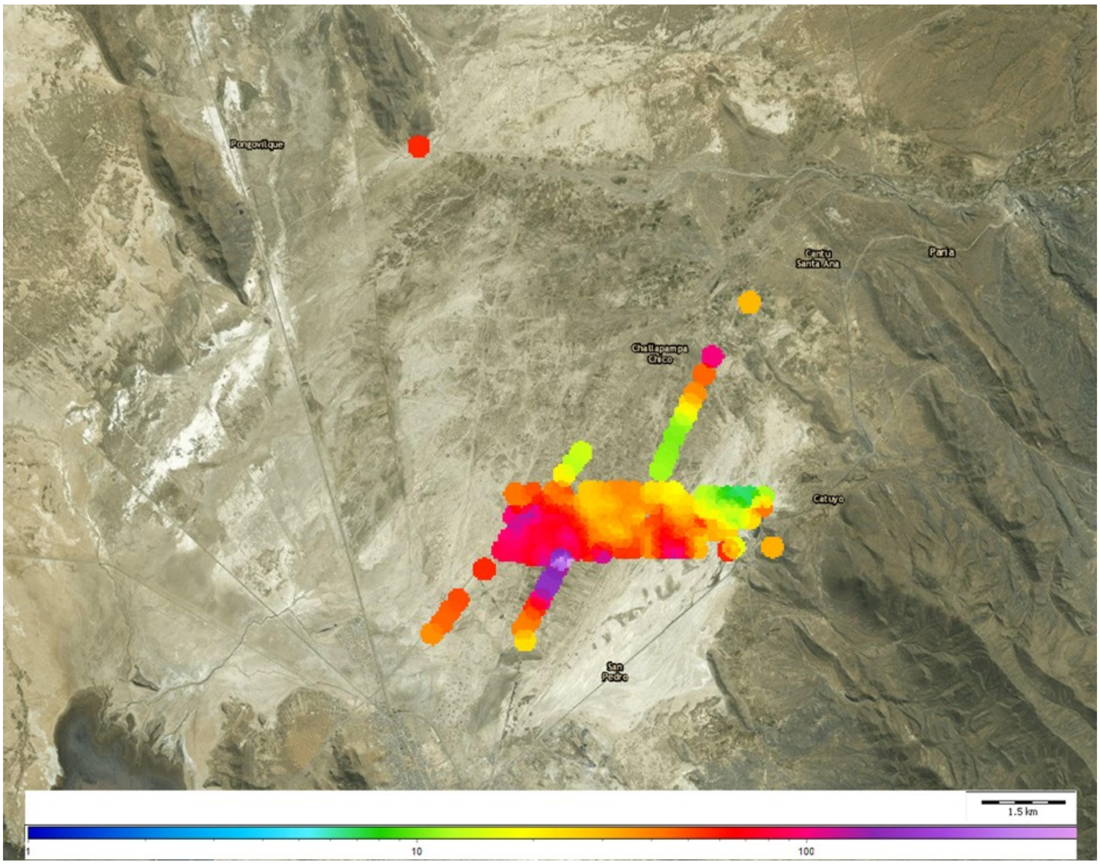

Fig. 19. Mean resistivity values for the interval 120-130 m b.s.

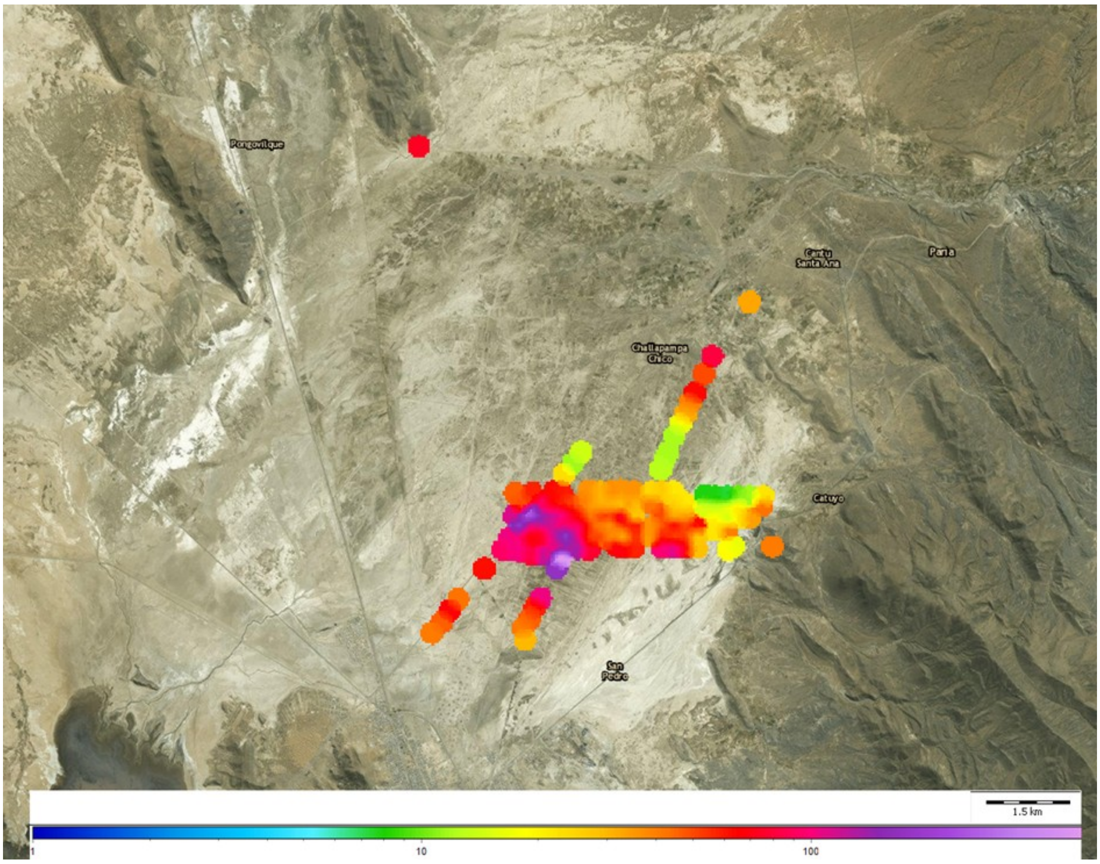

Fig. 20. Mean resistivity values for the interval 170-180 m b.s.

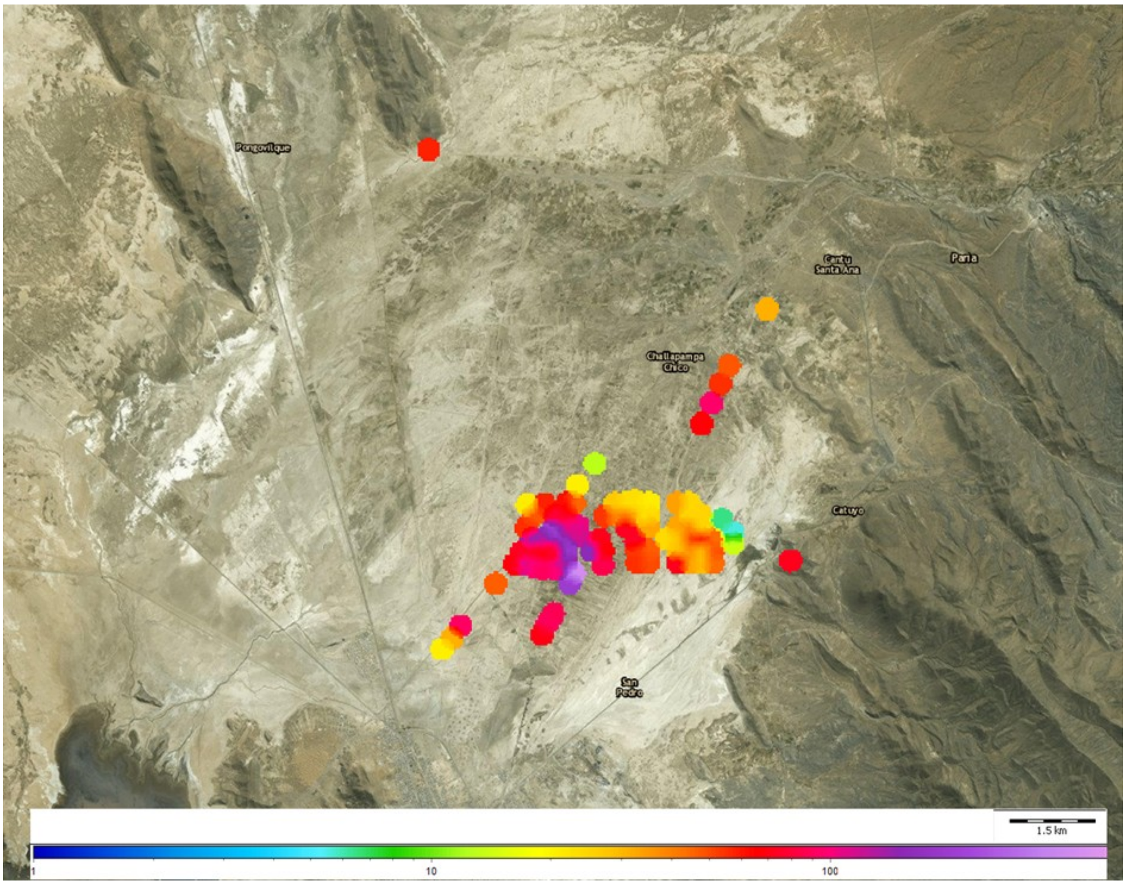

Fig. 21. Mean resistivity values for the interval 280-300 m b.s.

Three profiles, two in northeast to southwest directions and one from west to east (Fig. 15) are presented below. The three profiles were selected to highlight the trends recognized in the horizontal maps. All produced profiles and their location are in the appendix section (Fig. App. 6-8).

The westernmost profile (Profile 1), shows high resistivity values in its SW part and low values in the NE (Fig. 22). There is a transition from 20-30 Ωm to around 100 Ωm between 50-100 m b.s. in the southern part of the profile. There is a first indication of a high resistivity wedge between 1200-1600 m around 150 m b.s. and one very distinct high resistivity wedge between 3000-3800 m at 125 m b.s. This represents the highest resistivity values in the investigated area. The northern part of the profile shows low resistivity values between 10-30 Ωm down to 350 m b.s.

Profile 2 (Sne2; Fig. 15) is located east of profile 1. This profile shows a distinct resistivity drop between 1000-3400 m from 100-200 Ωm to 20-30 Ωm with great depth (Fig. 23). This correlates with the western

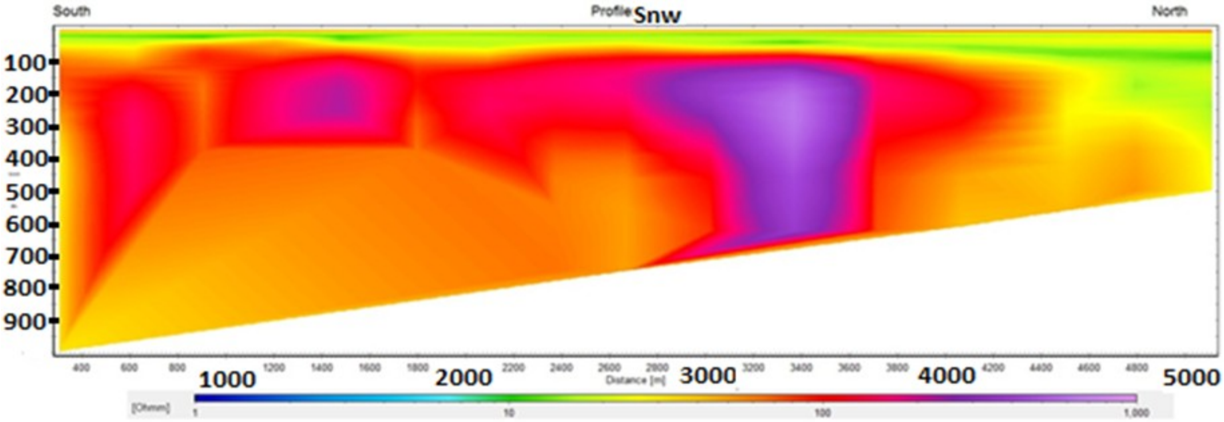

Fig. 22. Resistivity data for profile 1 (Snw). Interpreted depth is on the y-axis and distance is on the x-axis.

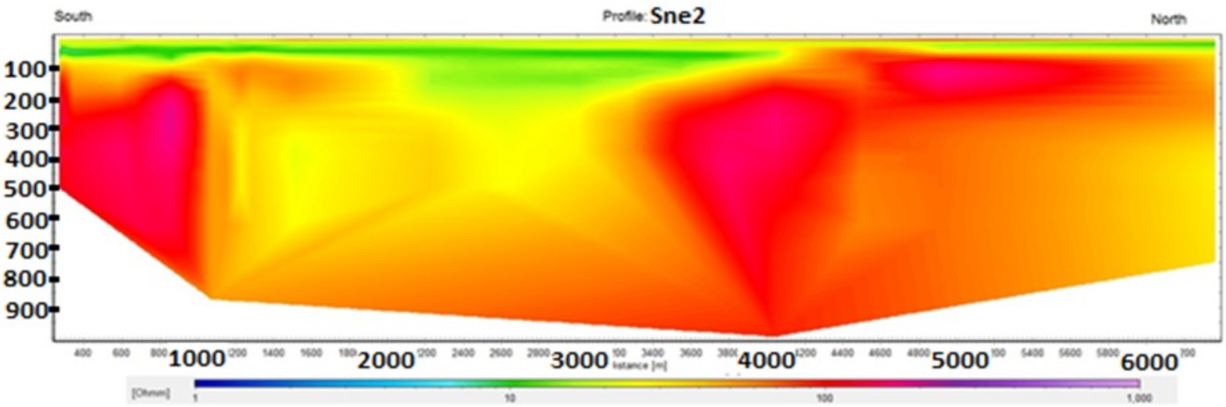

Fig. 23. Resistivity data for profile 2 (Sne 2). Interpreted depth is on the y-axis and distance is on the x-axis.

low resistivity value shown in Figs. 18 and 19. There is a shallow low resistivity valley situated on top of this resistivity drop with lower values to around 10 Ω m between 2000-3200 m with a lower limitation of 250 m b.s. The top layers have resistivity values at 10 Ωm until between 50-100 m b.s. This low resistivity layer is slightly thicker to the south but is interrupted at 4400 m, where it decreases in thickness to around 20 m b.s. and then increases slightly again towards northeast.

Profile 3 (northH2) was laid out from west to east (Fig. 15). At the western and eastern ends of this profile (Fig. 24) the resistivity increases from 10-20 Ωm to around 100 Ωm between 75-100 m b.s. The depth to increasing resistivity values increases towards the center of the profile. At 1700 m there is a low resistivity zone at the surface, continuing to 4800 m (Fig. 24). At 2900 m there is an indication of a slightly higher resistivity ridge at 60-70 Ωm that divides the low resistivity zone into two valleys. The top layers have higher resistivity to the west (around 100 Ωm) before entering the saturated sediments, and as low as 2 Ωm to the east. This is interpreted as due to the highly saline and water saturated sediments in the eastern part of the area. To the east there is a low resistivity zone (10 Ω m) down to 800 m b.s.

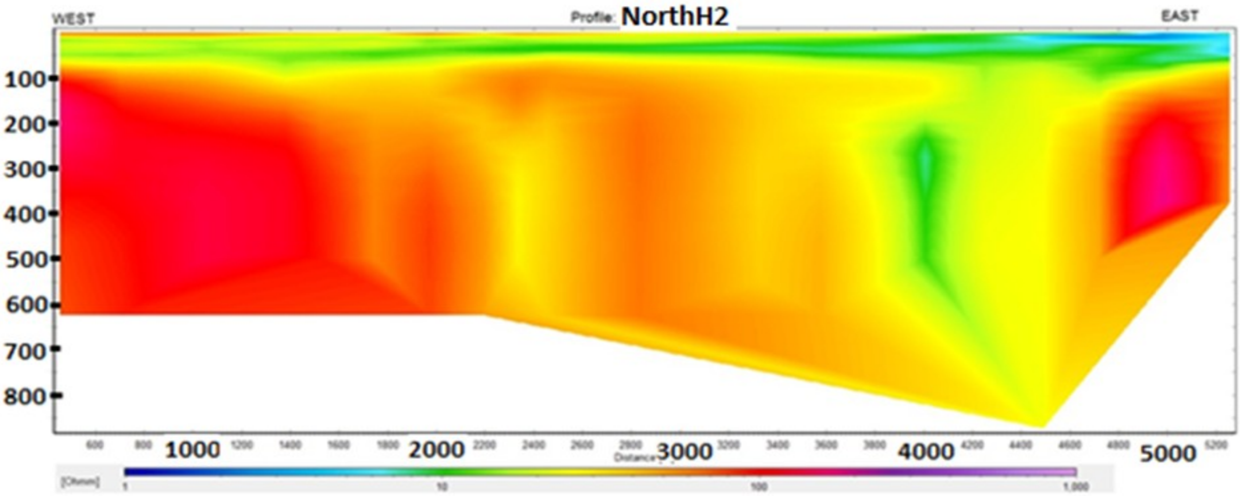

Fig. 24. Resistivity data for profile 3 (northH2). Interpreted depth on the y-axis and distance on the x-axis.

6 Discussion

The top 0-2 m interval of our surveyed sediments shows two high resistivity measurement points in the eastern part of the area (Fig. 16). These deviating resistivity values are probably due to the equivalence problem during the inversion of the measurement. The visualizations on the top layers (Figs. 16 and 17) are based on a layered model to make the transition from dry to water saturated sediments as visual as possible. On the smooth inversions, the resistivity values in the deviating points for this level are in line with its surrounding measurement, supporting the assumption that the deviating values in the layered inversions for this level are due to the equivalence problem.

In the western part of the area the average resistivity is higher than in the east but with a quite high degree of variation. The varying values are probably due to changes in the clay content in the top sediments. High clay content correlates with low resistivity values, and vice versa. A transition from dry surface sediments to saturated sediments is also clearly illustrated in the western part of the area. The dry surface sediments have resistivity values above 25 Ωm, correlating with clayey sand (Table 1). On the map for the thickness interval 10-12 m (Fig. 17) there is a distinct transition from dry sediments above 25 m to water saturated sediments around (resistivity ~10 Ωm). This correlates with the measured conductivity values for the second flow system (ii) with water conductivity between 0.06 and 0.2 S/m (5 - 16.7 Ωm). The very low resistivity values in the eastern part of the area for the same depth are most likely due to the increased salinity concentration. In this part the groundwater surface is at the same level as the ground surface, and due to the high evaporation during this season, the increased salt concentration explains the very low resistivity values at the top.

Both correlation points show resistivity values around 25 Ωm in the top 12 m (Fig. 16-17). This could be representative for a mix between dry sandstone and shale (Fig. 8). Both points show increases in resistivity with depth, but only the northern point keep an constant value of 100 Ωm after around 20 m b.s. This indicates fairly homogeneous bedrock to a depth of 470 m b.s. The outcrop adjacent to the northern point consists of the Catavi formation, which consists of sandstone.

The eastern correlation point shows variations between 25 to 200 Ωm from 12 m b.s. to 45 m b.s., and downwards between 200 to 40 Ωm down to 130 m b.s., and then to 100 Ωm again for 220 m b.s. These variations can have many explanations; grade of erosion, fractures, lithology, mineral content and presence of different pore fluids.

The resistivity changes in the northern reference point are most likely due to changes of lithology, fractures and mineral content. The low resistivity section in the top is probably linked to shale from the Silurian Uncía formation that is present in outcrops adjacent to this point. The high resistivity, starting at 45 m b.s., is hard to link to a specific formation but it could represent a transition from shale to sandstone or it could represent a transition to less fractured rock. The drop in resistivity at 130 m b.s. can be due to higher concentration of conductive minerals, or a transition back to shale dominated bedrock. At this level, the resistivity values are still higher than the interpreted resistivity for saturated rock, especially in this part where the groundwater is characterized by high concentration of salt. In both correlation points there are no resistivity values below 24 Ωm.

Two low resistivity valleys are shown in Fig. 18., extending in a northwest to southeast direction. The valleys have a signature resistivity of around 10 Ωm and are separated by a higher resistivity zone with values from around 25 to 90 Ωm. The western valley is extended to around 130 m b.s. along profile 3 before entering into what is interpreted as bedrock, as visible in Figs. 19 and 24. This valley dips towards northwest and extends all the way down to around 300 m b.s. in Figs. 21-22. The DOI is limited in the northern most point in Fig. 22. to around 300 m b.s., so below that the uncertainty if the data decreases.

The eastern low resistivity valley as shown in Fig. 18, extends to profile 2 (Sne2). In Fig. 23. the southern limitation of this valley is at 2 100 m and the northern at 4 000 m. The depth of the valley along the profile is around 250 m b.s. and the interpreted bedrock below has lower resistivity (25 Ωm) than the surrounding bedrock at but still falls within the values for the correlation points. Profile 3 (Fig. 24.) shows a depth of this valley to around 120 m b.s., this valley is also plunging towards northwest. Between 3 800 m and 4 500 m (Fig. 24) there is a wedge of low resistivity extending down to 850 m b.s. with resistivity values between 7-20 Ωm. It is unlikely that these values are linked to a sedimentary valley extending to that depth. The fact that this low resistivity wedge is situated adjacent to the hot springs and that there are intrusive bedrock in the close surrounding makes it highly likely that this low resistivity wedge represents an intrusion with higher concentrations of conductive minerals than in the surrounding rock.

A first indication of a high resistivity ridge is shown in the 120-130 m b.s. interval (Fig. 19), with resistivity values up to 1000 Ωm. The two interpreted peaks for this ridge are shown in Fig. 19. The orientation of the ridge shows up well on maps deeper than 130 m b.s in a northwest to southeast direction, just as the structures in the surrounding bedrock. In the profile presented in Fig. 22 the western ridge peak is at 100 m b.s., which is deeper than the eastern ridge top at around 70 m b.s.

7 Conclusions

- The TEM is a method well suited for investigating groundwater properties in sand- and gravel-dominated deposits. A depth of investigation (DOI) to 850 m b.s. was achieved in several points, which is over expectations. As the Challapampa aquifer is situated beneath a flat surface with low vegetation, it makes the measurements easy to setup and perform. A few power lines run through the area, but except for that there are almost no other sources for disturbance of the measurements.

- Saturated sediments have a signature resistivity below 25 m and are decreasing in resistivity with increasing salinity. The salinity is increasing towards the hot springs in the eastern part of the area.

- Interpreted bedrock has resistivities between 25 Ωm and 1000 Ωm. The large resistivity variations within bedrock are probably linked to different lithologies in which the maximum values are close to 1000 Ω m. The resistivity values of the correlation points are varying between 24-200 Ωm, which do is not representing intrusive rock.

- Low resistivity values, between 10-20 Ωm, encountered on greater depth in the eastern part of the studied area suggest intrusive rocks here. However, the low resistivity values can also be due to a higher geothermal gradient and/or salt content.

- Two low resistivity valleys, interpreted as water saturated sedimentary valleys, extend in a northwest to southeast direction over the studied area.

- The depth to the bedrock is interpreted to be around 75 m b.s., both in the western and eastern part of the area. The basal boundary for the interpreted sedimentary valleys crossing profile 3 (NorthH2, Fig. 24) is around 130 m b.s. for the eastern valley and 120 m b.s. for the western valley. From the horizontal maps and profile 2 it looks like the western valley is increasing in depth towards northwest. For the eastern valley it is harder to interpret a dip direction due to the highly conductive feature on greater depth for this part of the area.

- A ridge of high resistivity values in the western part of the study area is interpreted as bedrock influence. It has the same northwest to southeast direction as features in the surrounding mountainous area, and two peaks at 70 m b.s. and 100 m b.s.

- The Challapampita well field is situated on top of a bedrock ridge. The water production could be increased if extraction was moved into one of the sedimentary valleys more to the northeast. The Khala Kaja well field has overall better conditions for a higher water extraction from the aquifer.

8 Acknowledgment

A special thanks to following people: Etzar Gómez, Torleif Dhalin and Per Möller for supervising this thesis. I would also like to extend thanks to Rafael Mendoza Huayhua who was a reliable help during the field investigation.

This investigation had not been possible to perform whiteout the help from Nikolaj Foged and Esben Auken from Aarhus University, Denmark, regarding the TEM theory, configurations and support during the data evaluation process. I would also like to thank ABEM who supported us during the field campaign with a new instrument when the other instrument broke down.

I want to send my gratitude to the Technical Geology department in Lund, where I had a platform for developing discussions regarding problems, theories and assumptions.

9 References

Baker, P., Rigsby, C., Seltzer, G., Fritz, S., Lowenstein, T., Bacher, N., Veliz, C., 2001a. Tropical climate changes at millennial and orbital timescales on the Bolivian Altiplano. Nature 409: 698–701.

Baker, P., Seltzer, G., Fritz, S., Dunbar, R., Grove, M., Tapia, P., Cross, S., Rowe, H., Broda, J., 2001b. The history of South American precipitation for the past 25,000 years. Science 291: 640–643.

Banks, D., Holden, W., Aguilar, E., Mendez, C., Koller, D., Andia, Z., Rodriguez, J., Sæther, O. M., Torrico, A., Veneros, R. and Flores, J., 2002. Contaminant Source Characterization Of The San Jose Mine, Oruro, Bolivia.Geological Society, London, Special Publications 198.1: 215-239

Beck, A.E., 1981. Physical Principles of Exploration Methods", Macmillan, London.

Bills, B.G., de Silva, S.L., Currey, D.R., Emenger, R.S., Lillquist, K.D., Donnellan, A., Worden, B., 1994. Hydro-isostatic deflection and tectonic tilting in the central Andes: initial results of a GPS survey of Lake Minchinshorelines. Geophysical Research Letters 21: 293–296.

Christiansen, V. A., Auken, E., Sørensen, K., 2009. The transient electromagnetic method. I: R. Kirsch (red.): Groundwater geophysics a tool for hydrogeolog", 179-225. Berlin: Springer

Dames & Moore Norge., 1967. Comprehensive Evalúation of the Ground-Water Conditions, Challapampita Area". Oruro. Bolivia. Servicio Local dc Acueductos y Alcantarillado. Oruro.

Dames & Moore Norge., 2000. Informe Final 3, Resultados de las Investigaciones de Campo: Interpretación Hidrogeoquímica" ESTUDIO HIDROGEOLOGICO DE LA MINA SAN JOSE Y LOS ACUIFEROS QUE SUMINISTRAN AGUA A LA CIUDAD DE ORURO.

Fitterman, D. V. and Stewart, M. T., 1986. Transient Electromagnetic Sounding for Groundwater. Geology Faculty

Fritz, S.C., Baker, P.A., Lowenstein, T.K., Seltzer, G.O., Rigsby, C.A., Dwyer, G.S., Tapia, P., Arnold, K.K., Ku, T-L., Lou, S., 2004. Hydrology variability during the last 170,000 years in the southern hemisphere of South America. Quaternary Research 61: 95–104.

Gómez, E., Barmen, G., Rosberg, J,E., 2016. Groundwater Origins And Circulation Patterns Based On Isotopes In Challapampa Aquifer, Bolivia. Water 8.5: 207.

Grant, F.S., West, G.F., 1965. Interpretation Theory in Applied Geophysics. McGraw-Hill, New York, USA.

Lizarazu, J., Aranyossy, J.F., Orsag, V., Salazar, J.C., 1987. Estudio Isotopico de la cuenca de Oruro-Caracollo (Bolivia). In: Proceedings of Symposium of Isotope Techniques in Water Resources Development", Vienna,Austria, 30 March–3 April.

Loke, M.H., 2013. Tutorial 2-D and 3-D electrical imaging surveys. Dr. M.H.Loke. [pdf] <http://www.geotomosoft.com/coursenotes.zip> [20161001].

McNeill, J. D., 1980. Technical note TN-7 Application of transient electromagnetic techniques for resistivity sounding. Ontario: Geonics Limited <http://geonics.com/html/technicalnotes.html> [20161001].

McNeill, J. D., 1994. Technical note TN-27 Principles and application of time domain electromagnetic techniques". Ontario: Geonics Limited <http://geonics.com/html/technicalnotes.html> [20161001].

Menke, W., Menke, J., 2011. Environmental Data Analysis with MatLab. Academic Press, Elsevier Inc, Oxford UK, 263pp.

Nabighian, M.N., Macnae. J.C., 1991. Time domain electromagnetic prospecting methods. In: Nabighian, M.N. (Ed.): Electromagnetic methods in applied geophysics. Society of Exploration Geophysicists.

Palacky, G., 1987. Resistivity characteristics of geological targets, in electromagnetic methods in applied geophysics. Society of Exploration Geophysicists, 54-55.

Parker, R.L.,1994. *Geophysical Inverse Theory*. Princeton, N.J.: Princeton University, 400 pp.

Patureau, N., 2007. Contamination Of The Groundwater In Oruro City (Bolivia) And Possible Solutions To Avoid Polluting More In The Future. University of Newcastle upon Tyne.

Reading, H.G., 1986. Sedimentary Environments And Facies. Oxford: Blackwell Scientific, 615 pp.

Reineck, H-E.,Singh, I.G., 1975. Depositional Sedimentary Environments. Berlin, Heidelberg, New York: Springer, 439 pp.

Reynolds, J. M., 2011. "An Introduction to Applied and Enviromental Geophysics". Second edition. Oxford: John Wiley & Sons Ltd.

Rigsby, C. A., Bradbury, J. P., Baker, P. A., Rollins, S.

M., Warren, M. R., 2005. Late Quaternary Palaeolakes, Rivers, And Wetlands On The Bolivian Altiplano And Their Palaeoclimatic Implications. Journal of Quaternary Science 20, 671-691.

SCIDE, CORDEOR, & GEOBOL., 1981. “Proyecto de investigación y verificación de fuentes de abastecimiento de agua para la ciudad de Oruro”. Oruro.
SCIDE, Servicios de consultoria en ingenieria y desarrollo
CORDEOR, Cporporacion de desarrollo Oruro
GEOBOL, Servicio geologico de Bolivia

Sheriff, R.E., 2006. Encyclopedic Dictionary Of Applied Geophysics. Society of Exploration Geophysicists, 4th ed. Tulsa, Okla.

Sundberg, K., 1931. Gerlands Beitr. Geophysics. Ergänzungshefte, 1: 298-361.

Swedish Geological, A.B., 1992. Carta Geológica de Bolivia. Hoja Oruro, Publicación SGB Serie I-CGB-11. Servicio Geológico de Bolivia. Geobol; : La Paz, Bolivia.

Swedish Geological, A.B., 1996. Impacto de la Contaminación Minera e Industrial Sobre agua Subterráneas; Ministerio de Desarrollo Sostenible y Medio Ambiente, Secretaria Nacional de Mineria: Oruro, Bolivia.

University of Alberta, 2014 - University of Alberta, 2014. Resistivity of rocks and minerals. [pdf] <http://www.ualberta.ca/~unsworth/UA-classes/424/notes424/424B- 2014.pdf> [20161011].

10 Appendix

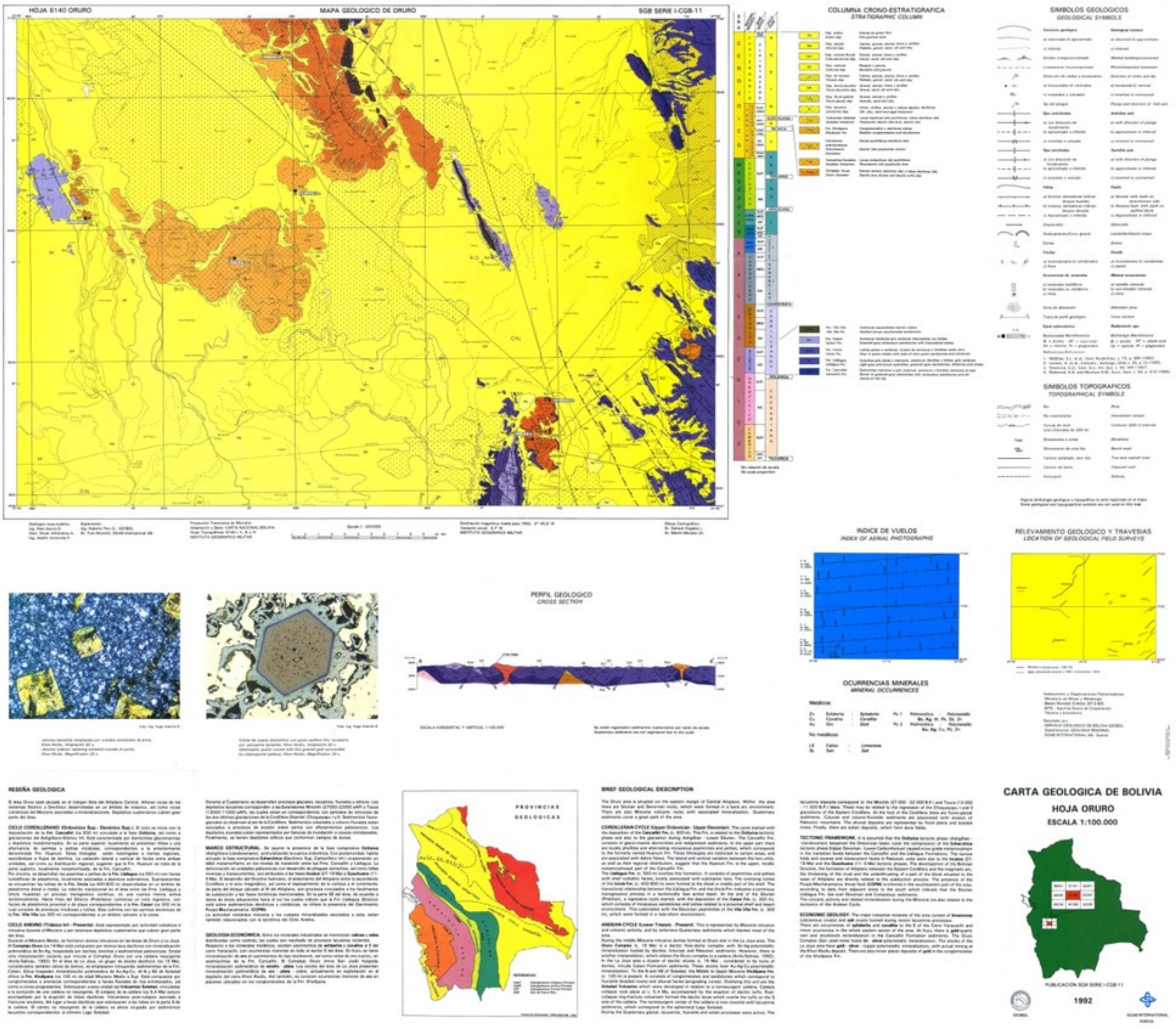

Fig. 1. Geological informational map of the investigated area with interpretations, produced by Swedish Geological AB, 1992.

Table 1. Drilling protocols with interpreted grain size distribution for every depth. Reference list is in the end of the table. Produced by the consulting companies: Scide et al. (1981).

PP_13							
start	end	cod_estrat	x	y	z	desde	hasta
0	11	64	699888	8022009	3705	3705	3694
11	26	46	699888	8022009	3705	3694	3679
26	31	463	699888	8022009	3705	3679	3674
31	36	46	699888	8022009	3705	3674	3669
36	43	34	699888	8022009	3705	3669	3662
43	46	436	699888	8022009	3705	3662	3659
46	50	346	699888	8022009	3705	3659	3655
50	51	463	699888	8022009	3705	3655	3654
51	52	46	699888	8022009	3705	3654	3653
52	53	463	699888	8022009	3705	3653	3652
53	69	346	699888	8022009	3705	3652	3636
69	72	463	699888	8022009	3705	3636	3633
72	77	643	699888	8022009	3705	3633	3628
77	80	346	699888	8022009	3705	3628	3625
80	83	643	699888	8022009	3705	3625	3622
83	85	346	699888	8022009	3705	3622	3620
85	86	643	699888	8022009	3705	3620	3619
86	87	346	699888	8022009	3705	3619	3618
87	88	364	699888	8022009	3705	3618	3617
88	92	346	699888	8022009	3705	3617	3613
92	93	436	699888	8022009	3705	3613	3612
93	96	346	699888	8022009	3705	3612	3609
96	102	643	699888	8022009	3705	3609	3603
102	107	463	699888	8022009	3705	3603	3598
107	110	643	699888	8022009	3705	3598	3595
110	111	346	699888	8022009	3705	3595	3594
111	129	643	699888	8022009	3705	3594	3576
129	130	463	699888	8022009	3705	3576	3575
130	133	64	699888	8022009	3705	3575	3572
133	154	463	699888	8022009	3705	3572	3551

PP_11							
start	end	cod_estrat	x	y	z	desde	hasta
0	1	65	701130	8023860	3707	3707	3706
1	3	46	701130	8023860	3707	3706	3704
3	24	456	701130	8023860	3707	3704	3683
24	30	43	701130	8023860	3707	3683	3677
30	38	435	701130	8023860	3707	3677	3669
38	40	436	701130	8023860	3707	3669	3667
40	42	34	701130	8023860	3707	3667	3665
42	45	346	701130	8023860	3707	3665	3662
45	50	36	701130	8023860	3707	3662	3657
50	63	346	701130	8023860	3707	3657	3644
63	64	365	701130	8023860	3707	3644	3643
64	71	346	701130	8023860	3707	3643	3636
71	73	36	701130	8023860	3707	3636	3634
73	80	364	701130	8023860	3707	3634	3627
80	90	346	701130	8023860	3707	3627	3617
SELA_2							
start	end	cod_estrat	x	y	z	desde	hasta
0	3	6	701937	8020922	3710	3710	3707
3	11	46	701937	8020922	3710	3707	3699
11	20	4	701937	8020922	3710	3699	3690
20	30	34	701937	8020922	3710	3690	3680
30	42	63	701937	8020922	3710	3680	3668
42	54	43	701937	8020922	3710	3668	3656
54	61	4	701937	8020922	3710	3656	3649
SELA_3							
start	end	cod_estrat	x	y	z	desde	hasta
0	2	6	701517	8020397	3711	3711	3709
2	20	46	701517	8020397	3711	3709	3691
20	32	43	701517	8020397	3711	3691	3679
32	51	4	701517	8020397	3711	3679	3660
51	64	3	701517	8020397	3711	3660	3647
SELA_4							
start	end	cod_estrat	x	y	z	desde	hasta
0	4	64	701167	8019989	3707	3707	3703
4	11	46	701167	8019989	3707	3703	3696
11	20	4	701167	8019989	3707	3696	3687
20	30	43	701167	8019989	3707	3687	3677
30	45	63	701167	8019989	3707	3677	3662
45	59	43	701167	8019989	3707	3662	3648
59	61	4	701167	8019989	3707	3648	3646
61	64	46	701167	8019989	3707	3646	3643

Reference			
type	cod		
boulder	1		
cobble	2		
gravel	3		
sand	4		
silt	5		
clay	6		
colloid	7		
rock	8		
examples			
	6	clay	
	26	cobble + clay	
	463	sand + clay + gravel	

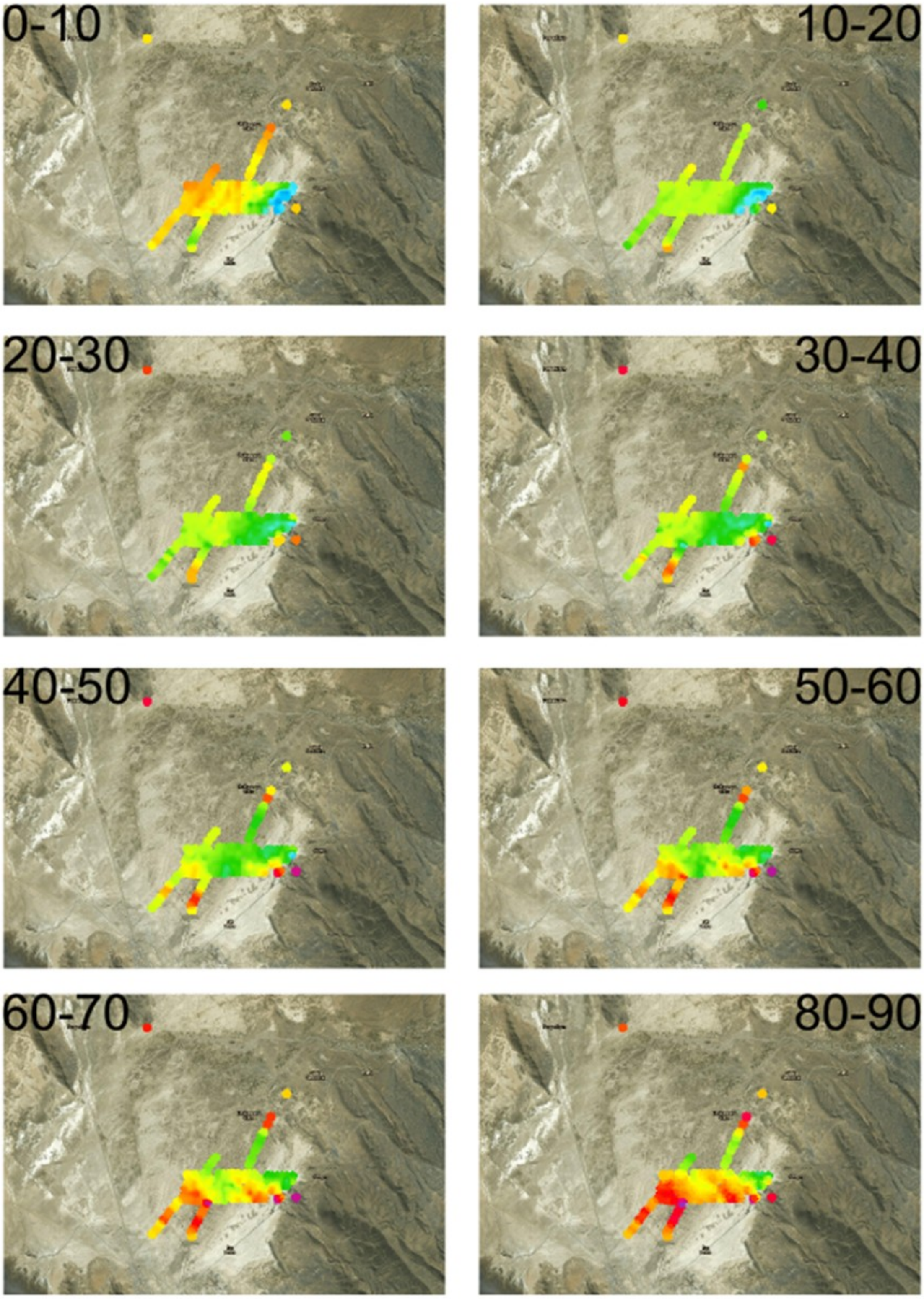

Fig. 2. Horizontal maps 10 m thick intervals from 0 m b.s. to 90 m b.s.

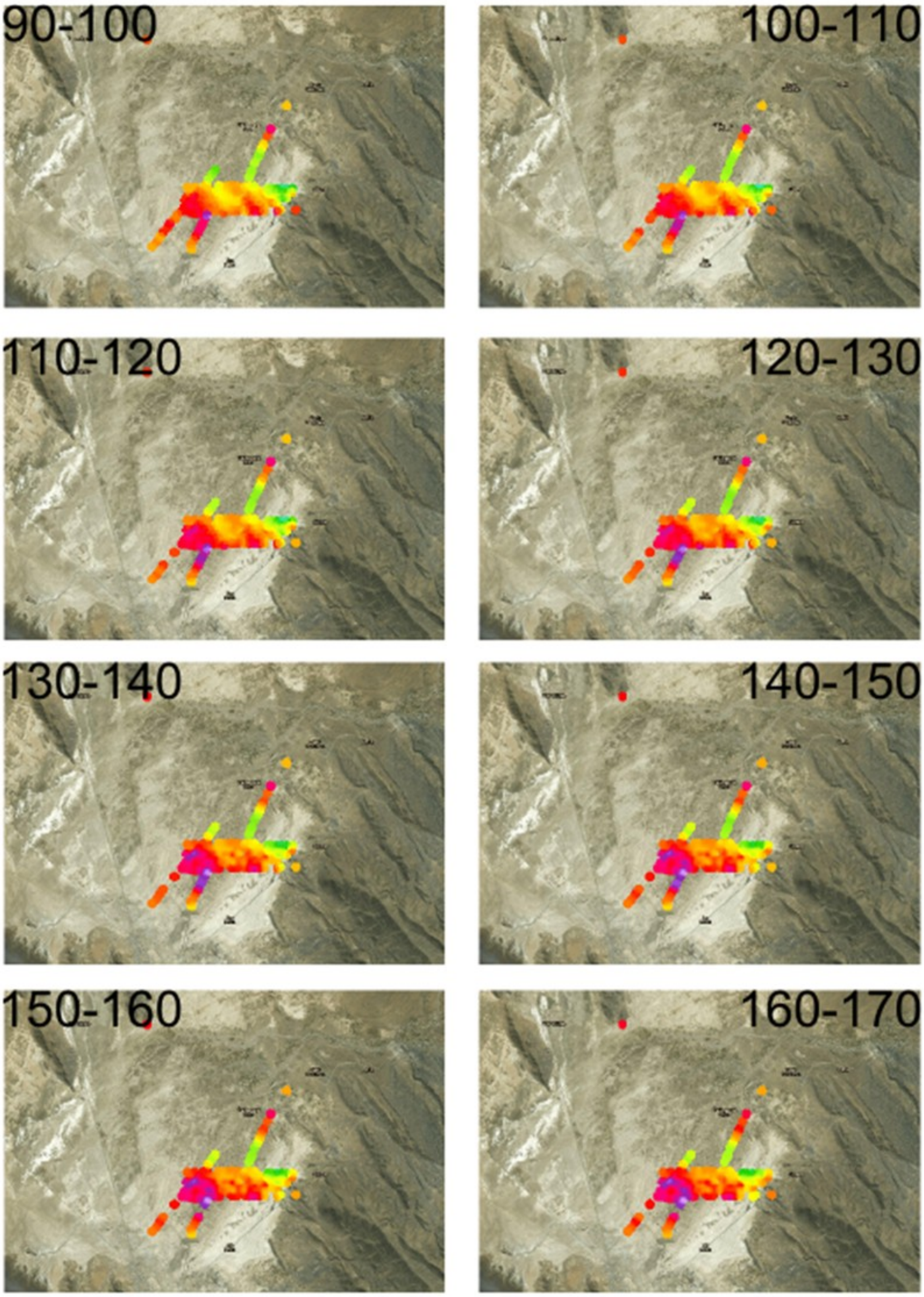

Fig. 3. Horizontal maps 10 m thick intervals from 90 m b.s. to 170 m b.s.

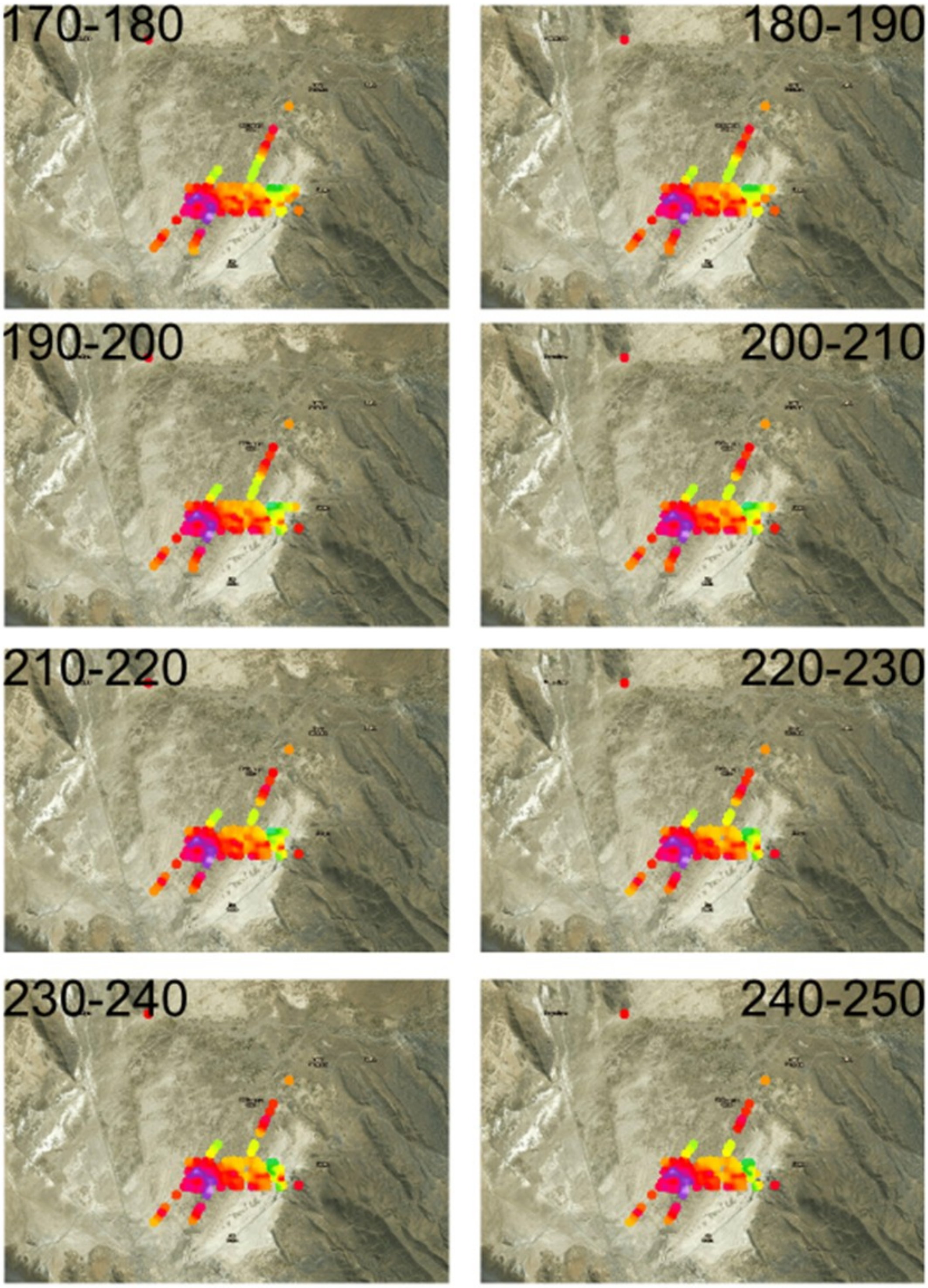

Fig. 4. Horizontal maps 10 m thick intervals from 170 m b.s. to 250 m b.s

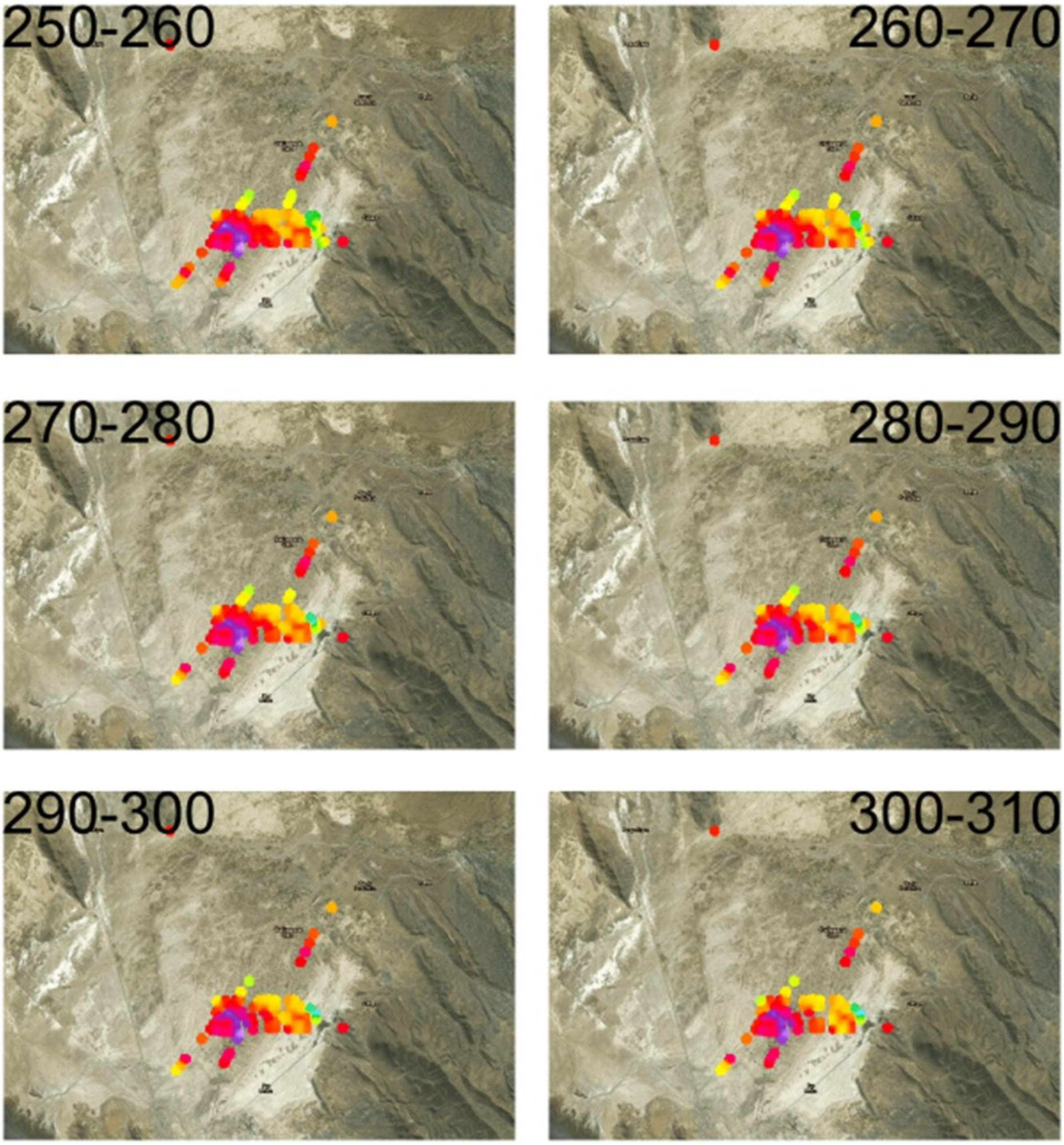

Fig. 5. Horizontal maps 10 m thick intervals from 250 m b.s. to 310 m b.s.

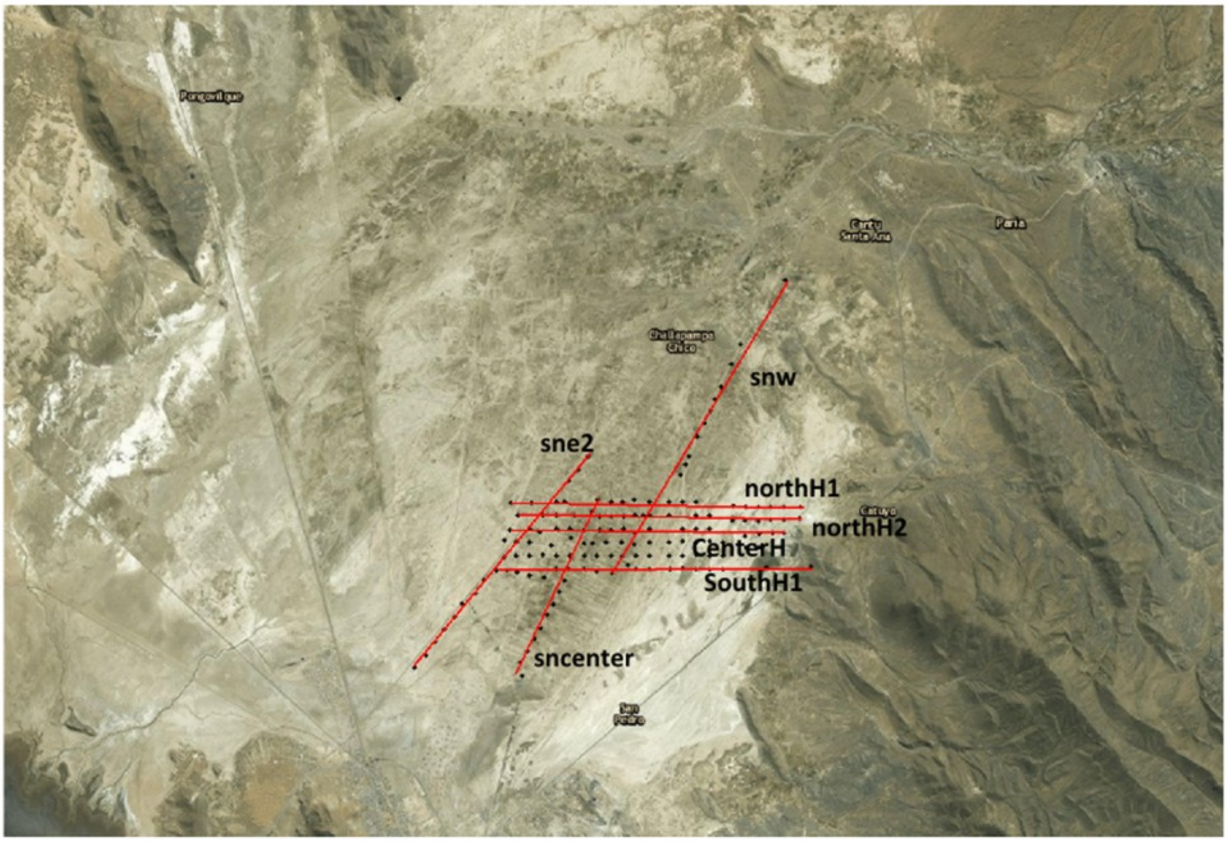

Fig. 6. Profile location names.

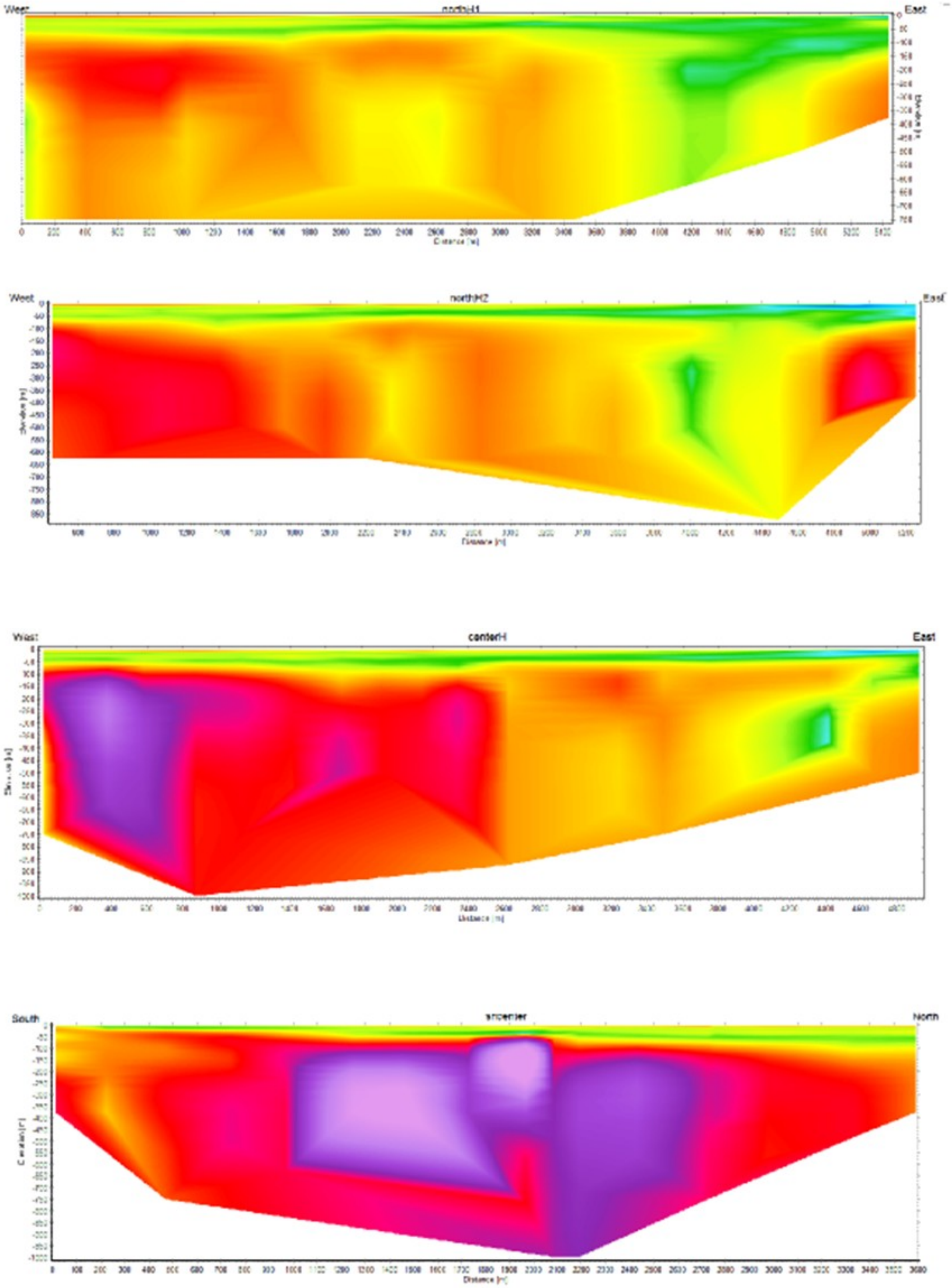

Fig. 7. Profiles in ascending order; northH1, northH2, CenterH and sncenter.

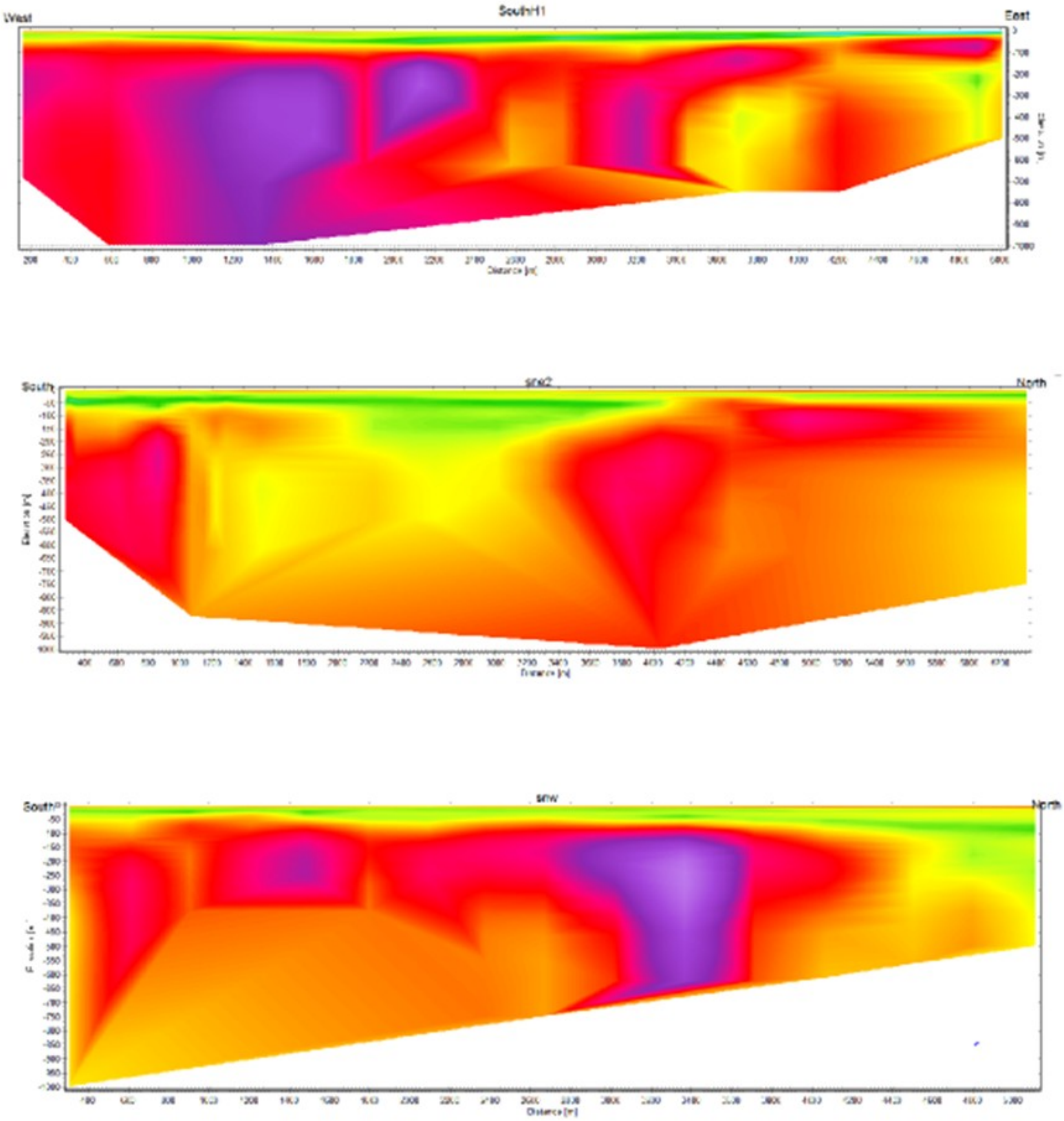

Fig. 8. Profiles in ascending order; SouthH1, sne2 and snw.

Tidigare skrifter i serien ”Examensarbeten i Geologi vid Lunds universitet”:

443. Lönsjö, Emma, 2015: Utbredningen av PFOS i Sverige och världen med fokus på grundvattnet – en litteraturstudie. (15 hp)
444. Asani, Besnik, 2015: A geophysical study of a drumlin in the Åsnen area, Småland, south Sweden. (15 hp)
445. Ohlin, Jeanette, 2015: Riskanalys över pesticidförekomst i enskilda brunnar i Sjöbo kommun. (15 hp)
446. Stevic, Marijana, 2015: Identification and environmental interpretation of microtextures on quartz grains from aeolian sediments - Brattforsheden and Vittskövle, Sweden. (15 hp)
447. Johansson, Ida, 2015: Is there an influence of solar activity on the North Atlantic Oscillation? A literature study of the forcing factors behind the North Atlantic Oscillation. (15 hp)
448. Halling, Jenny, 2015: Inventering av sprickmineraliseringar i en del av Sorgenfrei-Tornquistzonen, Dalby stenbrott, Skåne. (15 hp)
449. Nordas, Johan, 2015: A palynological study across the Ordovician Kinnekulle. (15 hp)
450. Åhlén, Alexandra, 2015: Carbonatites at the Alnö complex, Sweden and along the East African Rift: a literature review. (15 hp)
451. Andersson, Klara, 2015: Undersökning av slugtestsmetodik. (15 hp)
452. Ivarsson, Filip, 2015: Hur bildades Bushveldkomplexet? (15 hp)
453. Glommé, Alexandra, 2015: ^{87}Sr/^{86}Sr in plagioclase, evidence for a crustal origin of the Hakefjorden Complex, SW Sweden. (45 hp)
454. Kullberg, Sara, 2015: Using Fe-Ti oxides and trace element analysis to determine crystallization sequence of an anorthosite-norite intrusion, Älgön SW Sweden. (45 hp)
455. Gustafsson, Jon, 2015: När började plattektoniken? Bevis för plattektoniska processer i geologisk tid. (15 hp)
456. Bergqvist, Martina, 2015: Kan Ölands grundvatten öka vid en uppdämning av de utgrävda dikena genom strandvallarna på Ölands östkust? (15 hp)
457. Larsson, Emilie, 2015: U-Pb baddeleyite dating of intrusions in the south-easternmost Kaapvaal Craton (South Africa): revealing multiple events of dyke emplacement. (45 hp)
458. Zaman, Patrik, 2015: LiDAR mapping of presumed rock-cored drumlins in the Lake Åsnen area, Småland, South Sweden. (15 hp)
459. Aguilera Pradenas, Ariam, 2015: The formation mechanisms of Polycrystalline diamonds: diamondites and carbonados. (15 hp)
460. Viehweger, Bernhard, 2015: Sources and effects of short-term environmental changes in Gullmar Fjord, Sweden, inferred from the composition of sedimentary organic matter. (45 hp)
461. Bokhari Friberg, Yasmin, 2015: The paleoceanography of Kattegat during the last deglaciation from benthic foraminiferal stable isotopes. (45 hp)
462. Lundberg, Frans, 2016: Cambrian stratigraphy and depositional dynamics based on the Tomten-1 drill core, Falbygden, Västergötland, Sweden. (45 hp)
463. Flindt, Anne-Cécile, 2016: A pre-LGM sandur deposit at Fiskarheden, NW Dalarna - sedimentology and glaciotectonic deformation. (45 hp)
464. Karlatou-Charalampopoulou, Artemis, 2016: Vegetation responses to Late Glacial climate shifts as reflected in a high resolution pollen record from Blekinge, south-eastern Sweden, compared with responses of other climate proxies. (45 hp)
465. Hajny, Casandra, 2016: Sedimentological study of the Jurassic and Cretaceous sequence in the Revinge-1 core, Scania. (45 hp)
466. Linders, Wictor, 2016: U-Pb geochronology and geochemistry of host rocks to the Bastnäs-type REE mineralization in the Riddarhyttan area, west central Berglsagen, Sweden. (45 hp)
467. Olsson, Andreas, 2016: Metamorphic record of monazite in aluminous migmatitic gneisses at Stensjöstrand, Sveconorwegian orogen. (45 hp)
468. Liesirova, Tina, 2016: Oxygen and its impact on nitrification rates in aquatic sediments. (15 hp)
469. Perneby Molin, Susanna, 2016: Embryologi och tidig ontogeni hos mesozoiska fisködlor (Ichthyopterygia). (15 hp)
470. Benavides Höglund, Nikolas, 2016: Dig-

itization and interpretation of vintage 2D seismic reflection data from Hanö Bay, Sweden. (15 hp)

471. Malmgren, Johan, 2016: De mellankambriska oelandicuslagren på Öland - stratigrafi och faciestyper. (15 hp)

472. Fouskopoulos Larsson, Anna, 2016: XRF-studie av sedimentära borrkärnor - en metodikstudie av programvarorna Q-spec och Tray-sum. (15 hp)

473. Jansson, Robin, 2016: Är ERT och Tidsdomän IP potentiella karteringsverktyg inom miljögeologi? (15 hp)

474. Heger, Katja, 2016: Makrofossilanalys av sediment från det tidig-holocena undervattenslandskapet vid Haväng, östra Skåne. (15 hp)

475. Swierz, Pia, 2016: Utvärdering av vattenkemisk data från Borgholm kommun och dess relation till geologiska förhållanden och markanvändning. (15 hp)

476. Mårdh, Joakim, 2016: WalkTEM-undersökning vid Revingehed provpumpningsanläggning. (15 hp)

477. Rydberg, Elaine, 2016: Gummigranulat - En litteraturstudie över miljö- och hälsopåverkan vid användandet av gummigranulat. (15 hp)

478. Björnfors, Mark, 2016: Kusterosion och äldre kustdyners morfologi i Skälderviken. (15 hp)

479. Ringholm, Martin, 2016: Klimatutlöst matbrist i tidiga medeltida Europa, en jämförande studie mellan historiska dokument och paleoklimatarkiv. (15 hp)

480. Teilmann, Kim, 2016: Paleomagnetic dating of a mysterious lake record from the Kerguelen archipelago by matching to paleomagnetic field models. (15 hp)

481. Schönström, Jonas, 2016: Resistivitets- och markradarmätning i Ängelholmsområdet - undersökning av korrosiva markstrukturer kring vattenledningar. (15 hp)

482. Martell, Josefin, 2016: A study of shock-metamorphic features in zircon from the Siljan impact structure, Sweden. (15 hp)

483. Rosvall, Markus, 2016: Spår av himlakroppskollisioner - bergarter i nedslagskratrar med fokus på Mien, Småland. (15 hp)

484. Olausson, My, 2016: Resistivitets- och IP-mätningar på den nedlagda deponin Gustavsfält i Halmstad. (30 hp)

485. Plan, Anders, 2016: Markradar- och resistivitetsmätningar – undersökningar utav korrosionsförhöjande markegenskaper kring fjärrvärmeledningar i Ängelholm. (15 hp)

486. Jennerheim, Jessica, 2016: Evaluation of methods to characterise the geochemistry of limestone and its fracturing in connection to heating. (45 hp)

487. Olsson, Pontus, 2016: Ekologiskt vatten från Lilla Klåveröd: en riskinventering för skydd av grundvatten. (15 hp)

488. Henriksson, Oskar, 2016: The Dynamics of Beryllium 10 transport and deposition in lake sediments. (15 hp)

489. Brådenmark, Niklas, 2016: Lower to Middle Ordovician carbonate sedimentology and stratigraphy of the Pakri peninsula, north-western Estonia. (45 hp)

490. Karlsson, Michelle, 2016: Utvärdering av metoderna DCIP och CSIA för identifiering av nedbrytningszoner för klorerade lösningsmedel: En studie av Färgaren 3 i Kristianstad. (45 hp)

491. Elali, Mohammed, 2016: Flygsanddyners inre uppbyggnad – georadarundersökning. (15 hp)

492. Preis-Bergdahl, Daniel, 2016: Evaluation of DC Resistivity and Time-Domain IP Tomography for Bedrock Characterisation at Önneslöv, Southern Sweden. (45 hp)

493. Kristensson, Johan, 2016: Formation evaluation of the Jurassic Stø and Nordmela formations in exploration well 7220/8-1, Barents Sea, Norway. (45 hp)

494. Larsson, Måns, 2016: TEM investigation on Challapampa aquifer, Oruro Bolivia. (45 hp)

LUNDS UNIVERSITET

Geologiska institutionen
Lunds universitet
Sölvegatan 12, 223 62 Lund